



Final Draft **of the original manuscript**

Chernyshov, P.; Vrecica, T.; Streißer, M.; Carrasco, R.; Toledo, Y.:
**Rapid wavelet-based bathymetry inversion method for
nearshore X-band radars.**

In: Remote Sensing of Environment. Vol. 240 (2020) 111688.

First published online by Elsevier: 01.02.2020

<https://dx.doi.org/10.1016/j.rse.2020.111688>

Rapid Wavelet-based Bathymetry Inversion Method for Nearshore X-Band Radars

Pavel Chernyshov^{a,*}, Teodor Vrecica^a, Michael Streßer^b, Ruben Carrasco^b, Yaron Toledo^a

^aTel Aviv University, School of Mechanical Engineering, Tel Aviv 6997801, Israel

^bInstitute of Coastal Research, Helmholtz-Zentrum Geesthacht, Max-Planck-Straße 1, 21502 Geesthacht, Germany

Abstract

A wavelet based method for bathymetry retrieval from X-band radar images is proposed. The method combines traditional Fast Fourier Transform techniques for retrieving peak frequency maps by evaluating the spectral peaks in the time domain, and a localized 2D Continuous Wavelet Transform for retrieving the corresponding peak wavenumbers. The main improvements of the new method compared to conventional FFT-based methods are: a) the wavelet-based approach is localized - naturally fitting the inhomogeneous conditions typically found in the nearshore environment; b) it is continuous and uses wave phase information providing smooth bathymetry maps with good accuracy (RMSE in the range 2.6-6.6 percents of the maximum water depth); c) it requires relatively small number of successive images without the limitation of requiring a uniform time step.

In order to verify the proposed method, 2D simulations of wave shoaling and refraction were performed for different sea conditions and over several bottom topographies. A radar image model including tilt and shadowing modulations together with speckle noise was applied to the simulated surface elevations to provide synthetic radar images. The method's ability to reconstruct the original bathymetry is shown to be robust in intermediate to shallow water depths ($k_p h < 1$) for all cases. The method was also applied to real data acquired in Sylt island (Germany). A comparison between a bathymetric survey held prior to a storm and a radar reconstructed one during the storm shows very good agreement. These results reassure the high capability of this new method to be used in operational settings.

Keywords: Bathymetry reconstruction, X-band radar, wavelet analysis, shoaling waves

1. Introduction

Nautical X-band radars for measuring waves, currents and bathymetry are in growing use. This measurement method enables to study both the spatial and temporal evolution of waves, currents and bathymetries covering an area within a range of up to few kilometers. The knowledge of the sea bottom topography is crucial for a number of nearshore activities such as port and harbor operation, ship navigation, monitoring the influence of marine structures and scientific morphodynamic investigation. Indirect radio detection remote sensing methods have a number of advantages in comparison with traditional ship-based echo-sounding ones. Shipborne echo-sounder surveying provides quite good accuracy but has high operative costs which limit it to smaller areas and infrequent measurements even in the vicinity of harbours. The indirect remote sensing investigation is much cheaper and enables continuous measurements not only to snapshot the instantaneous bottom topography, but also to track its dynamics in time and space. Nautical X-band radars have reasonable accuracy and spatial resolution but still lower than echo-sounding. The sea surface range resolution is determined by the length of the transmitted electromagnetic pulse, and can be made small enough using

*Corresponding author

Email addresses: pavelc@mail.tau.ac.il (Pavel Chernyshov), vrecica@gmail.com (Teodor Vrecica), michael.stresser@hzg.de (Michael Streßer), ruben.carrasco@hzg.de (Ruben Carrasco), toledo@tau.ac.il (Yaron Toledo)

15 either short pulses or chirp pulse techniques. The azimuthal resolution is determined by the antenna’s beam width in the azimuthal plane (proportional to the antenna’s length), and the time lag corresponds to the antenna revolution period. The surface imaging is then analyzed based on wave propagation theory to provide the bathymetry maps.

20 One of the pioneering works on the estimation of the local bathymetry with X-band radar is (Bell, 1998, 1999), where the original approach of (Hart and Miskin, 1945) known from the 1940s was employed and developed in order to adapt it to X-band radar data (the original paper dealt with the aerophotography of the nearshore region). By analyzing the coherence of successive radar images, the local wave celerity was estimated. A simple linear theory formula, that neglects wave-current interactions, based on the ratio between wave celerities in deep water and local ones was used to calculate the water depths. In (Bell and Osler, 2011) the approach was considerably developed to be applicable also from a moving vessel.

25 The most common, conventional technique to estimate bathymetry and currents using X-band radars is based on the maximization of a functional representing the energy passed by the dispersion relation shell filter applied to the radar image’s 3D spectra with respect to depth and current’s vector (Hoogeboom et al., 1986; Piotrowski and Dugan, 2002). As an alternative technical realization of the mentioned idea, it is possible to use the approach of (Serafino et al., 2010), which minimizes the Normalized Scalar Product (NSP) functional with respect to the current vector and the local depth. This technique was applied quite 30 successfully to estimate the bathymetry in harbor areas (Ludeno et al., 2015). In (Ludeno et al., 2018) a sensitivity analysis of the NSP-based method was performed to evaluate how sea-state conditions and area partitioning affect bathymetric estimates. It also introduced an adaptive partitioning strategy that showed to give improved results. Nevertheless, these sort of the methods have the downside of needing a detailed resolution in the spectral domain both in wavenumbers and frequency. This requires using large 35 windows limiting the possibility to provide a high resolution bathymetry. It also assumes homogeneity which contradicts the nature of the shoaling wavefield especially for sharp bathymetry changes.

Another group of methods employs the best fit between two or more successive images using either the linear propagation operator $\Phi_{\pm}(k_x, k_y | d, \mathbf{u}) = e^{\pm i\omega(k_x, k_y | d, \mathbf{u})\tau}$ (Abileah and Trizna, 2010; Abileah, 2013; 40 Wang et al., 2015) or a Boussinesq model as an engine (Kennedy et al., 2000). Even though the methods were shown to give reasonably good results the thorough analysis of their performance with nearshore X-band radar data and their accuracy has not not been performed yet.

Several other works are worth mentioning. One of them, (Hessner et al., 1999), employed a Fourier analysis to extract the wave phase of the segregated harmonic with angular frequency ω_n as a function 45 of the wavenumber and spatial coordinates. The corresponding wavenumber is retrieved as a derivative with respect to the range vector $\mathbf{k}(\mathbf{r}, \omega_n) = \partial\Phi(\mathbf{k}, \mathbf{r}, \omega_n)/\partial\mathbf{r}$. This is valid only with the assumption that $\partial\mathbf{k}/\partial\mathbf{r} \ll 1$. Also in that work no wave-current interactions were taken into account. Similar, but more extended approach, called Dispersive Surface Classifier (DiSC) was proposed in (Senet et al., 2008). Another important work developed and tested a video image-based bathymetry reconstruction algorithm, 50 called “cBathy” (Holman et al., 2013). This is one of the most comprehensive works combining several signal processing approaches such as Fourier transform, frequency dependent empirical orthogonal functions (EOF) and Kalman filtration to fill the gaps in spatial coverage. The retrieved bathymetries were tested in time and space versus CRAB (Coastal Research Amphibious Buggy) surveys (Birkemeier and Mason, 1984). In (Rutten et al., 2017), the accuracy was evaluated by comparing the correspondent FFT-based 55 X-band radar images derived bathymetry with cBathy - Argus video system based - algorithm. Results show significant biases of radar derived bathymetries in shallow waters ($h < 6$ m).

It is important to observe that most of the above bathymetry inversion methods do not perform an analysis to quantify the error associated with Doppler shift due to currents. The only attempt to address the problem was made in (Honegger, 2015), where it was found that the corresponding error cannot be 60 always neglected. Although not for the bathymetry inversion problem, the limitation of Fourier analysis to treat inhomogeneous signals was pointed out several times before, e.g. (Chuang et al., 2008; Wu et al., 2011; Chernyshov et al., 2018). In those works, in order to overcome the above limitation for the analysis of wave shoaling over a slightly varying topography, the 1D and 2D CWT (Continuous Wavelet Transform) were employed.

65 The 2D CWT was tested recently as a tool for inversion of the bathymetry profiles in nearshore environ-

ments (Poupardin et al., 2016). The method is designed to reconstruct the bathymetry from two successive optical SPOT-5 satellite images with different spatial resolution separated by a time lag Δt of 2.04 s. Although the method was able to reconstruct nearshore bathymetry using such poor data, one of its downsides is that, if several wavemodes are used for the bathymetry estimation, it is not clear *a-priori* which estimate is more robust, introducing uncertainty in the bathymetry estimation.

As seen from the above works, the wavelet method shows great promise for nearshore inhomogenous conditions, nevertheless the wavelet method has not yet been adopted for bathymetry retrieval from nearshore X-band radar data images. The main objective of this paper is to fill this gap by developing and testing a 2D CWT-based method of bathymetry inversion for both synthetic (modeled) radar images and real data.

The main idea of the new method is to track the position of the spectral peak in a wavevector domain as a function of the spatial coordinates, while waves are shoaling and refracting towards the shore. The corresponding celerities are retrieved by dividing the phase shift in space by a known time lag and averaging it within an image time sequence. This approach allows to retrieve not only the wavevector modulus but its angle as well. This provides the additional capability to incorporate ambient current field retrieved by conventional radar (see e.g. (Huang et al., 2016)) or other alternative means.

The paper is structured as follows: in Section 2 the sea surface simulation stochastic approach is described. Section 3 introduces the main radar imaging mechanisms. Section 4 is dedicated to the theoretical introduction and definitions pertinent to the 2D CWT. It is followed by Section 5 giving the detailed description of the new 2D CWT-based bathymetry inversion method. The results analysis is resumed in Sections 6 and 7 for synthetic and real data cases respectively. The paper is finalized by discussion and conclusions in Section 8 and Appendix with two additional method's tests.

2. 2D sea surface simulations for shoaling conditions

In this section a linear method for sea surface simulation is outlined. The bathymetry, initial conditions, and governing equations used in the simulation are presented. Some of the underlying assumptions are discussed at the end of the section.

The original formulation of the JONSWAP (JOint North Sea WAVE Project) spectra $S(f)$ (see (Hasselmann et al., 1973)) is used to define the energy distribution across frequencies. The input parameters of the JONSWAP spectra for all simulations and the resulting wave parameters are given in Table 1. In order to better resolve the spectral peak, an elimination method sometimes referred to as Neuman's method (see e.g. (Litvenko and Prigarin, 2014)) is used. This method is generally employed to model random values with continuous distribution density functions defined on an infinite interval (e.g. Gaussian distribution). In this particular case, a simplified version of the method is utilized. Since it is assumed that most of the wave energy density is localized in a reasonably small interval near the spectral peak, the majoring function can be a constant. The frequency is modeled in accordance with a distribution proportional to the wave amplitude spectrum rather than the energy density in order to increase the number of points near the spectral tail. A brief description of the elimination algorithm can be given as follows. First, a uniformly distributed random value in the interval $a = [0, \sqrt{S(f_p)}]$ is generated. Next, a loop that provides a uniformly distributed random frequency within the interval $[f_{min}, f_{max}]$ is run until it provides one whose energy density is larger than that of a^2 , in which case it is eliminated. This is shown schematically in Figure 1 (a). A total of one hundred frequencies were determined this way in each simulation.

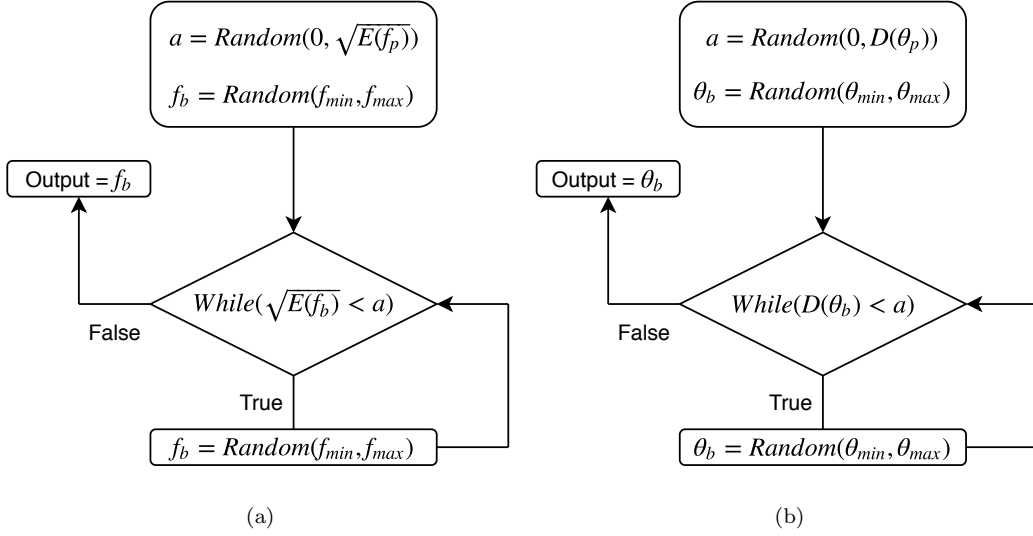


Figure 1: Flowchart of the peak elimination method for (a) frequency definition and for (b) direction definition.

The directional wave properties are described using a Mitsuyasu frequency dependent spread function (see (Mitsuyasu et al., 1975)) defined as:

$$D(f, \theta) = \frac{2^{2s-1} \Gamma^2(s+1)}{\pi \Gamma(2s+1)} \left| \cos((\theta - \theta_p)/2) \right|^{2s}, \quad (1)$$

where

$$s = \begin{cases} s(f/f_p)^5, & \text{if } f < f_p, \\ s(f/f_p)^{-2.5}, & \text{if } f > f_p. \end{cases} \quad (2)$$

The spread width near the peak frequency direction θ_p is controlled using the parameter

$$s = c(2\pi f_p U_{10}/g)^{-2.5}, \quad (3)$$

where U_{10} represents the mean wind speed at 10m height, f_p is the peak frequency, g is the acceleration of gravity, and a constant $c = 30$ is taken in order to represent a narrow spectral width. The elimination method is also used in a similar manner (refer to Figure 1 (b)) to define forty directional components for each of the chosen frequencies. This process results in a much better frequency resolution near the frequency-direction peak (Figure 2).

The initial individual wave amplitudes are defined as follows:

$$a_{nm}(\mathbf{0}) = \sqrt{2 \int_{(f_n+f_{n-1})/2}^{(f_n+f_{n+1})/2} \int_{(\theta_m+\theta_{m-1})/2}^{(\theta_m+\theta_{m+1})/2} S(f, \theta) df d\theta}. \quad (4)$$

The bathymetry is defined as that of a mildly changing beach:

$$h(x, y) = \begin{cases} 1/2(2000 - x)^{2/3}, & x \leq 1800(\text{m}), \\ 17.1 \times 10^{-(x-1800)0.00113}, & x > 1800(\text{m}), \end{cases} \quad (5)$$

with depth value expressed in meters (Figure 3). The bathymetry is based on an equilibrium beach profile (see (Bruun, 1954)) joined by a mild slope leading into shallow water. It is assumed there are no lateral changes to the beach profile.

A linear formulation of the mild slope equation is used to simulate the sea surface elevation in space and time ($\eta(x, y, t)$). The sea surface is modeled using a quasi-2D approach (see, e.g., (Chuang et al., 2008; Wu et al., 2011; Bredmose et al., 2005)), which accounts for refraction and shoaling effects. At this stage, for the sea surface simulation, we assume the origin of the physical space coordinate system to be in deep water, with positive x pointing towards the shore, positive z pointing strictly upwards, and positive y directed in such a way that (x, y, z) form a right-hand triple. Further, $\mathbf{0}$ is referred to as the origin in deep water (Figure 3). In this case, the sea surface elevation is defined as the following linear superposition of the frequency-direction wave components

$$\eta(x, y, t) = \Re \left[\sum_{n=1}^{N_\omega} \sum_{m=1}^{N_\theta} a_{nm}(x, y) e^{-i(\omega_n t - k_{y_{nm}} y - \int_0^x k_{x_{nm}}(\xi) d\xi + \varphi_{nm})} \right], \quad (6)$$

where $k_{y_{nm}}(x, y) = k_n(\mathbf{0}) \sin(\theta_m(\mathbf{0}))$ is the lateral wave number, $k_{x_{nm}}(x, y) = k_n(x, y) \cos(\theta_m(x, y))$ is the onshore wave number, $a_{nm}(x, y)$ is the wave amplitude (Equation (4)), φ_{nm} is the initial random phase uniformly distributed over $[0, 2\pi)$, and $\omega_n = 2\pi f_n$ is the angular wave frequency and f_n defined with the elimination method above. The angular frequency and the wave number satisfy the dispersion relation

$$\omega_n^2 = gk_n(x, y) \tanh(k_n(x, y)h(x, y)), \quad (7)$$

115 which is used to define the wave number $k_n(x, y)$ as a solution of Equation (7) at every point in the spatial domain. It is important to notice that, within the linear theory framework, the angular frequency of a monochromatic wave remains constant in space by virtue of the wave conservation law (Dean and Dalrymple, 1991).

In order to describe the linear shoaling of the wave field, the following equation is used:

$$a_{nm}(x, y) = a_{mn}(\mathbf{0}) \sqrt{\frac{C_{g_{nm}}^x(\mathbf{0})}{C_{g_{nm}}^x(x, y)}}, \quad (8)$$

where $C_{g_{nm}}^x$ is the onshore group velocity. It is expressed as

$$C_{g_{nm}}^x(x, y) = \frac{\omega_n}{2k_n(x, y)} \left(1 + \frac{2k_n(x, y)h(x, y)}{\sinh(2k_n(x, y)h(x, y))} \right) \cos(\theta_m(x, y)), \quad (9)$$

120 with $\theta_m(x, y) = \arcsin(\sin(\theta_m(\mathbf{0}))k_n(\mathbf{0})/k_n(x, y))$ as defined by Snell's law (Dean and Dalrymple, 1991). Since a laterally uniform bathymetry function was used, the y coordinated might be omitted in all definitions. It is nevertheless kept here to be applicable in a general case.

125 The exponential term in Equation (6) represents the phase function of every harmonic, describing its oscillations in time and space. The linear energy flux is conserved through the ratio of onshore group velocities. For a quasi-2D bathymetry, the refraction is modeled with the integral of the onshore wavenumber in the exponent power of Equation (4). The onshore wavenumber grows in shallower water, while the lateral wavenumber remains constant, leading to a shift of wave direction towards the shoreline.

130 The effects of wave reflection and nonlinearity are important for the overall evolution of the wave field, however they do not significantly affect the position of the primary frequency peak for realistic wave spectra. As only the information on the primary peak is needed for bathymetry inversion purposes, these effects are not considered further. This also assumes that the nonlinearity leading to formation of coherent patterns is weak, and that waves are mostly sinusoidal. In many realistic cases, coherent patterns will form in shallower waters. This topic is left for a future investigation.

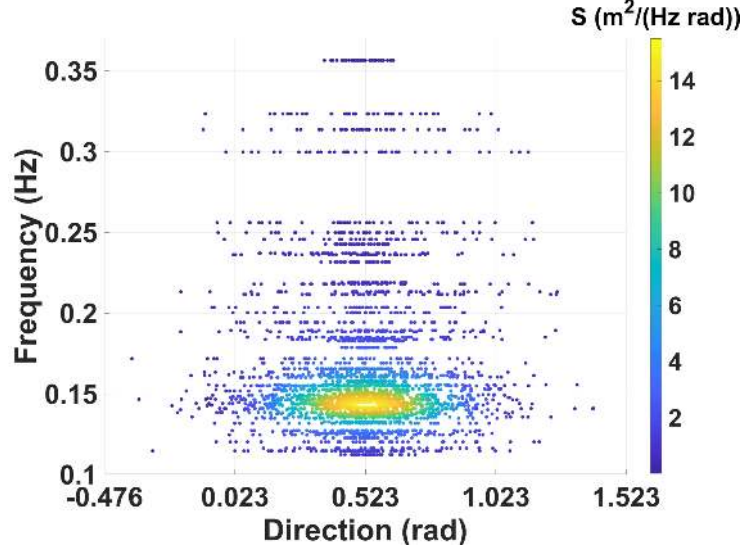


Figure 2: Point plot of the discretized wave spectra. The spectra is discretized in four thousand frequency directional bins, as outlined in Section 3. The color indicates the energy density at each point.

Sea surface images are constructed using Equation (6) with a 2-second time step for a total of 200 seconds. The incident wave peak in deep water propagates at a $\theta_p(\mathbf{0}) = 30^\circ$ angle. As waves approach the coastline the wave field starts to bend towards it, propagating almost perpendicularly to it near the shore. Wave amplitudes are also changed due to shoaling effects.

135

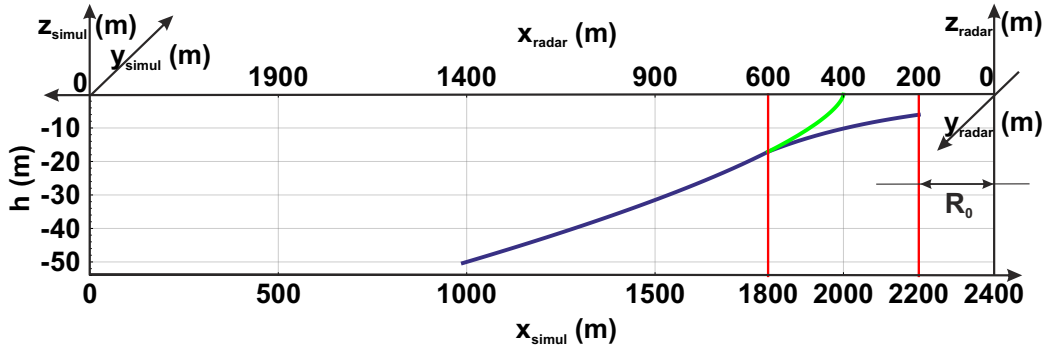


Figure 3: Bathymetry profile according to Equation (5) as a function of the simulation (x_{simul}) coordinate and the corresponding x coordinate for radar image construction stage (x_{radar}). The green extension of the original equilibrium profile shows how it evolves to the zero depth. Red vertical lines denote the change of the profile type and the offset R_0 used in the radar image simulation

To simplify the radar image modeling, in following sections the spatial coordinate origin is redefined as the radar installation point (see Figure 3). To ensure the image is in the far zone of the radar, an offset R_0 is added (here $R_0 = 200$ m). In Figure 4 the corresponding sea surface elevation is given as a function of the new coordinates.

Table 1: JONSWAP spectrum parameters used for surface modeling.

Parameter	Value
fetch (F)	500 (km)
peak enhancement factor	3.3
wind speed (U_{10})	3.2, 9.2 (m/s)
peak period (T_p)	7, 10 (s)
initial significant wave height ($H_s(\mathbf{0})$)	1.76, 4.53 (m)
time step (dt)	2 (s)
spatial step (dx, dy)	5 (m)
number of frequencies (N_ω)	100
number of directions (N_θ)	40
number of time samples (N_t)	100
number of range samples (N_x)	243
number of azimuth samples (N_y)	201

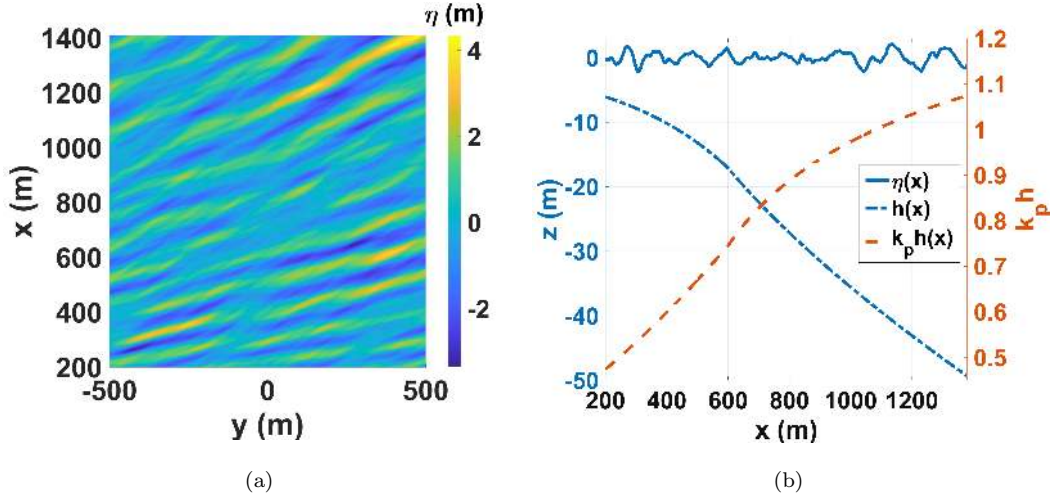


Figure 4: (a) An example of JONSWAP spectrum-based 2D shoaling wavefield (bottom view); (b) The bathymetry profile defined in Equation (5) (dash-dotted blue line), the relative water depth ($k_p h$) (dashed orange line), and 1D sea surface elevation (solid blue line). The coordinate system is already changed to radar one as described in Figure 3. The shortening of the wavelength together with a mild amplitude modulation is clearly visible while entering shallower waters.

140 3. 2D radar image simulations

Radar image simulations are generally conducted following the well-known approach initially proposed in (Borge et al., 2004), and developed in (Salcedo-Sanz et al., 2015). Its main steps, which have also been followed in this paper with minor modifications, are:

- 145 • *Simulation of the shadowing mask.* The shadowing, which is a partial occultation of the wave due to the presence of longer waves, is considered to be one of the dominant imaging mechanism for grazing incidence. Numerically, the shadowing area is evaluated using a simple criterion based on the comparison between local incidence angles for each couple of range points in all direction (see Figure 5 (a)) (Borge et al., 2004).

150 • *Tilt modulation simulation.* Tilt modulation appears due to changes in the effective incidence angle of the Bragg resonant ripples over long wave profiles. The maximum tilt modulation intensity is assumed to be on the side of the profile facing the radar, hence it provides a constant phase shift equal to $\pi/2$ relative to the original surface elevation profile. Numerically it is evaluated as a scalar product between the unitary external normal vector and the unitary vector pointing to the radar antenna taken at the same point on the surface.

155 • *Speckle noise addition.* Speckle noise is a multiplicative noise characteristic of all coherent systems. Its multiplicative nature is due to the fact that the radar signal, scattered from a part of the wave profile, returns already modulated by the orbital velocities of the long waves (Kanevsky, 2008).

• *The radar equation.* The classical form of the radar equation (see, e.g., (Skolnik, 1970)) gives the received power P_{rec} as

$$P_{rec}(\mathbf{r}) = \frac{P_{trans}GA_{eff}\sigma}{16\pi^2R^4}, \quad (10)$$

where P_{trans} is the transmitted power (W), G is the antenna gain coefficient, $R = \sqrt{H_r^2 + \mathbf{r}^2}$ is the distance (m), A_{eff} is the antenna effective aperture area (m^2), and σ is the target cross-section (m^2).

160 When the same antenna is used to both transmit and receive, the transmitting gain G and the effective receiving aperture A_{eff} are related by $G = 4\pi A_{eff}/\lambda_{em}^2$, where λ_{em} is the length of the radar electromagnetic wave. Hence, everything on the right-hand-side of Equation (10), except for σ and R^{-4} , can be included as a constant.

165 Equation (10) can be represented in terms of intensity $I(r) \propto I_0/R^3$ (here, I_0 is a reference intensity), since the pixel size is equal to $r\Delta r\Delta\phi$ and grows with R (Δr and $\Delta\phi$ are the range and the azimuthal resolution, respectively). This equation can be used to subtract the range trend in a real images. However, in the simulation cases the effect of the radar equation can be disregarded.

The final formula for the corresponding reference intensity looks as follows:

$$I_{tilt+sh} = \begin{cases} (\mathbf{n} \cdot \mathbf{u}), & \text{if } (\mathbf{n} \cdot \mathbf{u}) > 0 \text{ and no shadowing occurs,} \\ 0, & \text{otherwise.} \end{cases} \quad (11)$$

170 In this case the speckle noise is added using the following model $I_{tilt+sh+sn} = (I_{tilt+sh} + c_1)(1 + nlG)$, where c_1 is a constant offset, added in order to control the signal to noise ratio, G is a realization of the standard Gaussian noise, nl is the desired noise level ($0 \leq nl \leq 1$), which will be further expressed in percents for convenience.

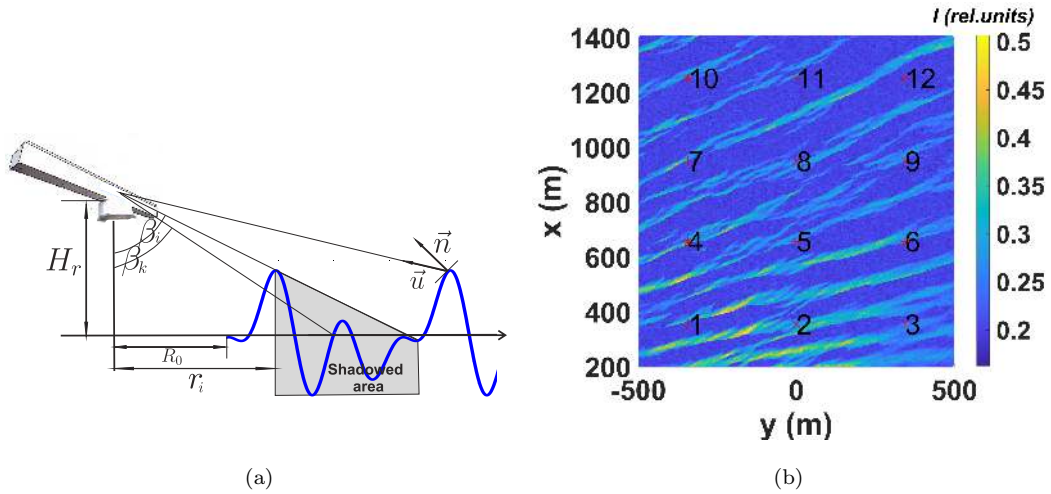


Figure 5: (a) Probing geometry scheme including the illustration of shadowing and tilt modulation as a scalar product of the unitary external normal vector \mathbf{n} and the unitary vector pointing to the radar antenna \mathbf{u} ; (b) An example of radar image with $H_r = 20$ m, noise level 5 % (intensity is given in relative units). Stars and numbers correspond to the numbering of probing locations for 2D CWTF, given in Figure (7).

The result of the described procedure applied to the original surface elevation from Figure 4 (a) is given in Figure 5 (b). The correspondent wavelet spectra at different points of the image are given in Figure 7.

4. Theoretical background for two dimensional continuous wavelet transform (2D CWT)

175 In this section the theoretical background and definitions regarding the mathematical basis of the Continuous Wavelet Transform will be given. The wavefield in shoaling conditions, regarded as a stochastic process, does not fulfill the stationarity requirement in space. Mathematically, the spatial stationarity of a random process $\{X(\mathbf{r}_i)\}_{i=1}^{N_r}$ in a broad sense requires the existence of the mathematical expectancy MX and the dispersion $DX \neq 0$, both non depending on a position of the point $\mathbf{r}_i = (x_i, y_i)$; in addition it assumes
180 the existence of the covariance function $\text{cov}(X(\mathbf{r}_i), X(\mathbf{r}_j)) = K(\mathbf{r}_i, \mathbf{r}_j) = \tilde{K}(\mathbf{r}_i - \mathbf{r}_j)$ which depends on the difference, but not the points' positions themselves. For linear shoaling conditions, the sea surface elevation as a random function of space does not fulfill this definition due to the fact that, for instance, the dispersion DX is not constant. Therefore, the sea surface elevation distribution can be considered to be locally Gaussian and stationary in time but not in space. More precisely, the time propagation of a stochastic process
185 $\{X(\mathbf{r}_i)\}(t)$ regarded as a function of time for a certain \mathbf{r}_i will be a Gaussian, locally stationary process.

Due to the fact that wavelengths shorten during shoaling in the shallow water area, the sea surface elevation can not be considered to be a periodic signal either. Both these statements imply the inapplicability of the traditional Fourier analysis in a global image. Hence, an alternative approach using a two dimensional continuous wavelet transform will be employed. This principally allows to localize spectral analysis in a
190 spatial domain using the correlation of the analyzed signal and a mother wavelet, which can be scaled, shifted and rotated. The rotation allows to resolve the directional properties of the signal, providing that the mother wavelet itself is anisotropic (Antoine and Murenzi, 1996). The analyzed signal is a spatial radar image $I(\mathbf{r})$ is assumed to be squarely integrable, which means that its $L_2(\mathbb{R}^2)$ norm is finite $\|I(\mathbf{r})\|_{L_2(\mathbb{R}^2)}^2 = \int_{\mathbb{R}^2} |I(\mathbf{r})|^2 d\mathbf{r} < \infty$. The mother wavelet is defined by assuming $\psi \in L_2(\mathbb{R}^2)$ and that the admissibility
195 condition is satisfied (Daubechies, 1992):

$$C_\psi = (2\pi)^2 \int_{\mathbb{R}^2} |\xi|^{-2} |\hat{\psi}(\xi)|^2 d\xi < \infty, \quad (12)$$

or, equivalently $\int_{\mathbb{R}^2} \psi(\boldsymbol{\xi}) d\boldsymbol{\xi} = 0$. To be able to employ the mother wavelet ψ in 2D space a triply-indexed families of wavelets, dilations, rotations and translations are added:

$$\psi_{a,\mathbf{b},\theta}(\mathbf{r}) = a^{-1} \psi \left[\mathbf{R}_\theta^{-1} \left(\frac{\mathbf{r} - \mathbf{b}}{a} \right) \right],$$

where $a \in \mathbb{R}_+$ serves for the dilation of the mother wavelet (scaling factor), $\mathbf{b} \in \mathbb{R}^2$ is a position vector, $\mathbf{R}_\theta \in SO(2)$ is a standard rotation matrix of a rotating angle θ . Once the appropriate mother wavelet $\psi(\mathbf{r})$ is chosen, the 2D CWT of a signal $I(\mathbf{r})$ can be defined as follows:

$$W[I(\mathbf{r}), \psi(\mathbf{r})](a, \mathbf{b}, \theta) = C_\psi^{-1/2} a^{-1} \int_{\mathbb{R}^2} I(\mathbf{r}) \psi_{a,\mathbf{b},\theta}^*(\mathbf{r}) d\mathbf{r}, \quad (13)$$

where the asterisk denotes the complex conjugate.

In linear water wave theory applications, the Morlet mother wavelet is usually used. The 2D Morlet wavelet is a direct extension of the 1D one to the spatial case and is represented in the following form:

$$\psi(x, y) = \frac{1}{\sqrt{2\varepsilon\sigma^2}} e^{-ik_0x} e^{-1/2\sigma^2(x^2/2+(y/\varepsilon)^2)}, \quad (14)$$

where k_0 is the central wavenumber (frequency), ε is the anisotropy parameter, and σ is the shape parameter. In the Fourier domain, Equation (14) is

$$\hat{\psi}(k_x, k_y) = e^{-\sigma^2((k_x - k_0)^2 + (\varepsilon k_y)^2/2)}. \quad (15)$$

Typically the triple $(k_0, \sigma, \varepsilon) = (6, 1, 1)$ is taken. For the following analysis to better resolve the directionally narrow wavefield the triple $(k_0, \sigma, \varepsilon) = (6, 1, 2)$ with increased anisotropy parameter will be employed.

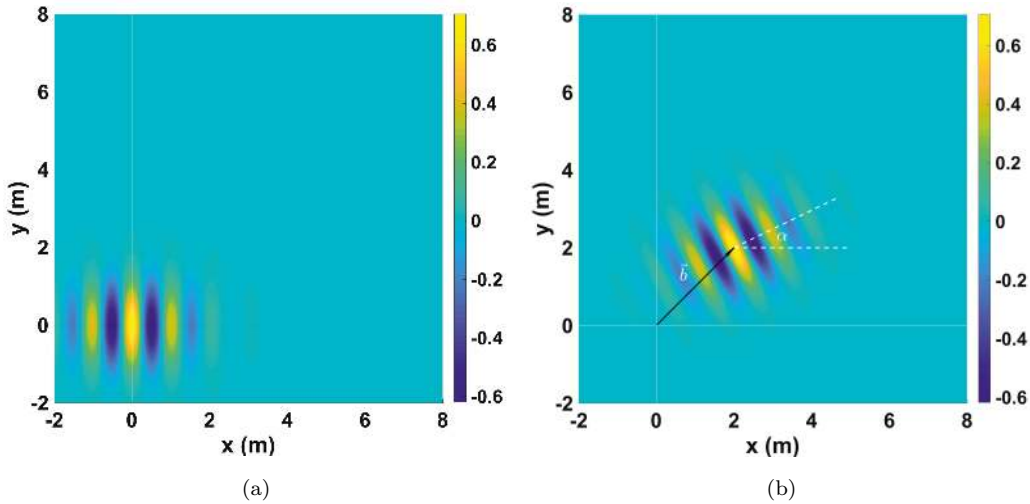


Figure 6: (a) Original Morlet wavelet in the physical (x, y) space (see Equation 14); (b) The same Morlet wavelet rotated ($\alpha = \pi/7$) and translated $\mathbf{b} = (2, 2)$.

To optimize the numerical realization of the 2D CWT, the following identical representation of Equation (13) is commonly used (Wang and Lu, 2010)

$$W[I(\mathbf{r}), \psi(\mathbf{r})](a, \mathbf{b}, \theta) = C_\psi^{-1/2} a \int_{\mathbb{R}^2} \hat{I}(\mathbf{k}) \hat{\psi}^*(a\mathbf{R}_\theta^{-1}(\mathbf{k})) e^{i\mathbf{b}\mathbf{k}} d\mathbf{k}, \quad (16)$$

which allows to replace the heavy calculation of the double integral in Equation (13) with the calculation of two direct and one inverse 2D Fourier transforms.

The following transformation from the pair (a, θ) to the pair (k_x, k_y) will be useful in the following sections. As for the 1D CWT, the relationship between the pseudo-wavenumber and the scaling factor is defined as

$$|\mathbf{k}| = \frac{k_0}{dx \cdot a}, \quad (17)$$

205 where dx is the corresponding spatial resolution (refer to Table 1). In this paper, the same resolution is used in range and azimuth directions $dx = dy = 5$ m, hence it becomes very easy to calculate the wavevector $\mathbf{k} = (k_x, k_y) = (|\mathbf{k}| \cos(\theta), |\mathbf{k}| \sin(\theta))$, where θ is taken from the set of angles defined for the rotations of the mother wavelet (spectral directions set). Resulting 2D and 1D (spectral angle-integrated) wavelet spectra are given in Figures 7 and 8.

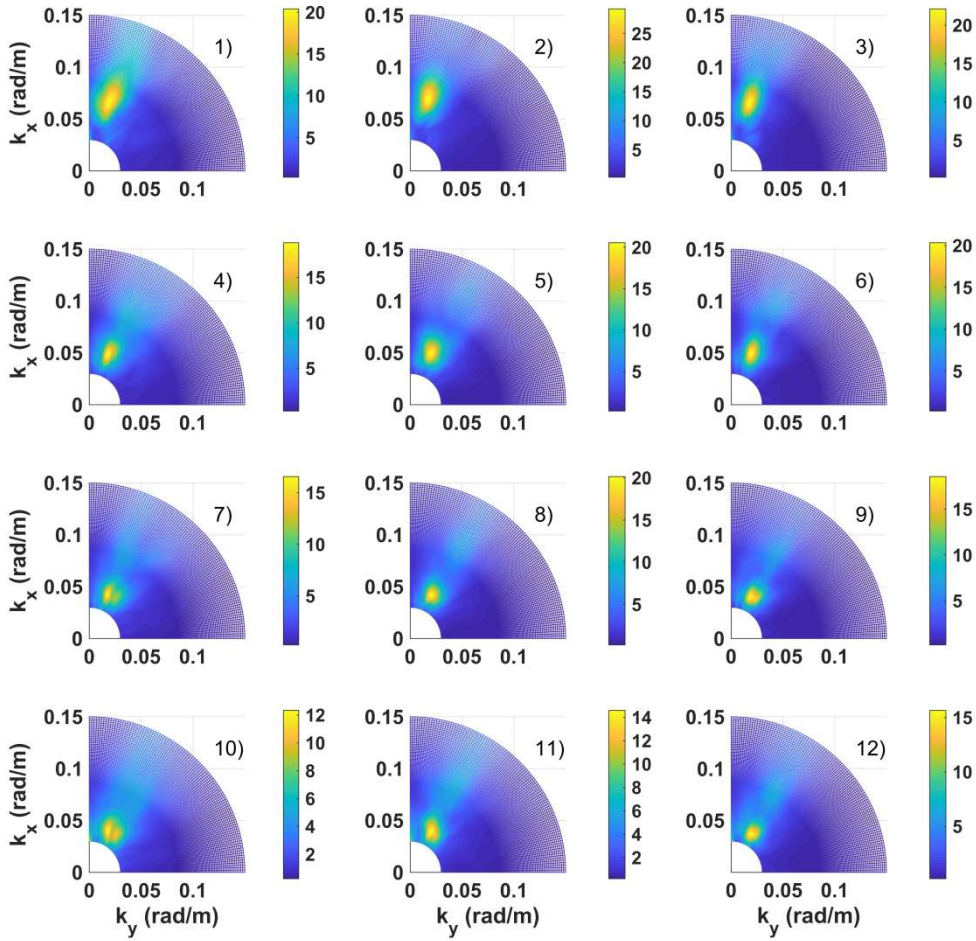


Figure 7: The wavelet spectra of the radar image, averaged over one hundred time samples (200 s). The numbering corresponds to the probing locations given in Figure 5 (b). All the phenomena taken into account in the simulations are obviously visible: refraction (the incidence angle tends to decrease), shoaling (wave shortening - wavenumber growth), the second harmonic due to the presence of shadowing is also clearly seen.

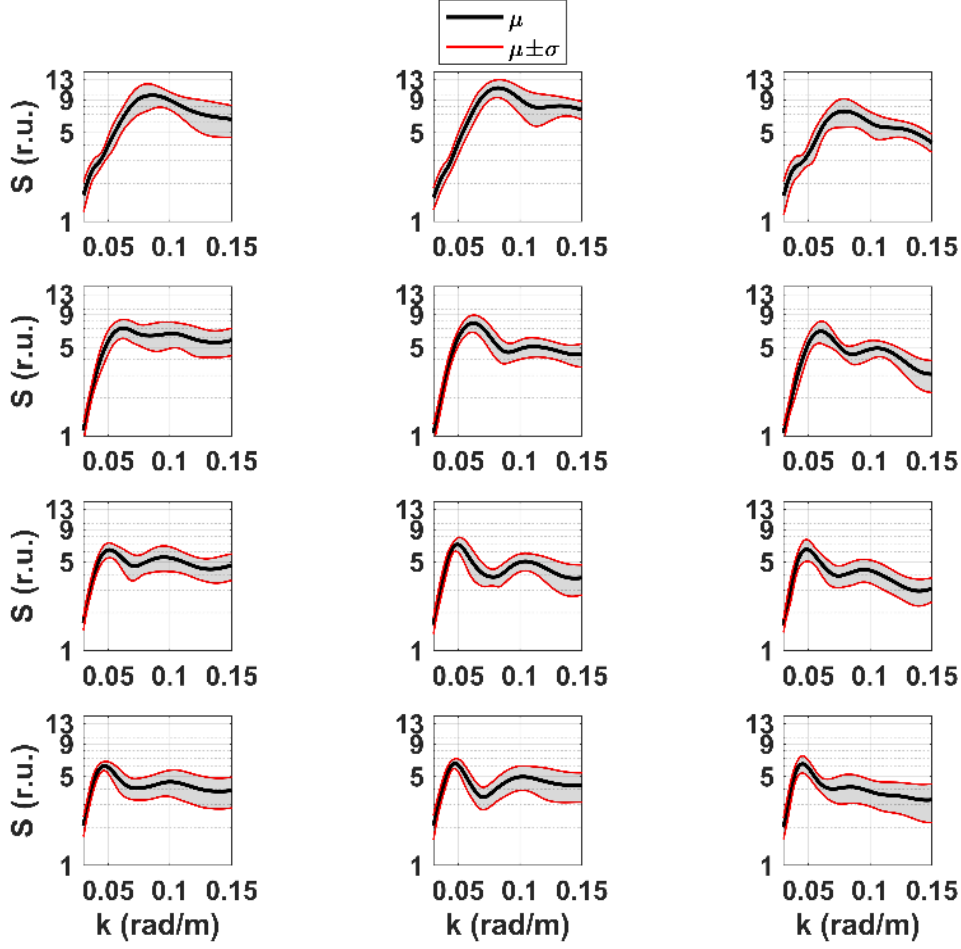


Figure 8: The 1D omnidirectional (spectral angle-integrated) wavelet spectra with the corresponding mean (black solid line μ) and standard deviation limits (gray zone with the red St.D. limits $\mu \pm \sigma$). The order of spectra corresponds to that in Figure 7. Spectral values are given in relative units (r.u.).

210 5. Bathymetry reconstruction technique

In this section, a 2D Rapid Wavelet-based Bathymetry Inversion (RWBI) method for bathymetry reconstruction is presented. Unlike the traditional FFT analysis approach, the 2D CWTFT is employed to estimate the peak wavenumber as a function of space $\mathbf{k}_p(\mathbf{r})$. In (Hessner et al., 1999) and (Poupardin et al., 2016) it was proposed to track any wavenumber $\mathbf{k}(\mathbf{r}, \omega_n)$ in space. Here, without loss of generality, 215 it is suggested to track only the peak spectral component $\mathbf{k}_p(\mathbf{r}) = \mathbf{k}(\mathbf{r}, \omega_p)$. The dominant wave period $T_p(\mathbf{r})$ is assumed to be almost constant and will be used to empirically estimate the scaling factor vector, corresponding to the primary peak component.

The reconstruction procedure includes the following steps:

1. Estimation of the peak period T_p from the radar or other independent measurements. The corresponding scaling factors' vector is estimated as follows:

$$a \in [a_{min}, a_{max}] = k_0 T_p^2 / dx [1/15, 1/3] \quad (18)$$

2. Ramp (range trend) subtraction in order to make the mean radar image intensity level to be more homogeneous in space

$$\tilde{I}_n(\mathbf{r}) = I_n(\mathbf{r}) - \frac{1}{N_t} \sum_{i=1}^{N_t} I_i(\mathbf{r}), \quad n = 1, \dots, N_t. \quad (19)$$

3. Estimation of the 2D CWTFT coefficients transforming a set of corresponding successive radar images $\{\tilde{I}_n(\mathbf{r})\}_{n=1}^{N_t}$ to a set of local directional complex wavelet spectra $\{W(\mathbf{r}, t_n | \mathbf{k}, \theta)\}_{n=1}^{N_t}$.
4. Averaging of the corresponding wavelet spectral information among several neighboring pixels for computational cost reduction (optional). If n_a is the number of averaging pixels in both directions, n_a^2 pixels will be averaged. $W(\mathbf{r}, t_n | \mathbf{k}, \theta) \mapsto \tilde{W}(\tilde{\mathbf{r}}, t_n | \mathbf{k}, \theta)$. Here $\tilde{\mathbf{r}}$ is the redefined grid, in which each point corresponds to the center of mass of the averaged pixels. For brevity it will be denoted as \mathbf{r} , remembering that it is already a redefined spatial grid. This step is optional and might be skipped if there is no lack of RAM and hard drive (HD) space to save heavy spectral files.
5. Averaging of the resulting wavelet spectral information in time in order to get smoother spectral peak estimation

$$W_{av}(\mathbf{r}, |\mathbf{k}|, \theta) = 1/N_t \sum_{n=1}^{N_t} \left| \tilde{W}(\mathbf{r}, t_n | \mathbf{k}, \theta) \right|.$$

6. Determination of the peak wavevector $\mathbf{k}_p(\mathbf{r}) = \underset{(|\mathbf{k}|, \theta)}{\operatorname{argmax}} |W_{av}(\tilde{\mathbf{r}}, |\mathbf{k}|, \theta)|$.
7. Calculation of the corresponding celerities based on the phase shifts (dl).

$$dl(\mathbf{r}, t_n) = \arg \left(\tilde{W}(\mathbf{r}, t_n | \mathbf{k}_p, \theta_p) \tilde{W}^*(\mathbf{r}, t_{n+1} | \mathbf{k}_p, \theta_p) \right) / |\mathbf{k}_p| \quad (20)$$

The time average of the celerities is obtained as $c_p(\mathbf{r}) = \frac{1}{N_t dt} \sum_{n=1}^{N_t-1} dl(\mathbf{r}, t_n)$

8. The solution of the corresponding dispersion relation to resolve depths

$$h(\mathbf{r}) = \left| \frac{\tanh^{-1}(c_p^2(\mathbf{r}) |\mathbf{k}_p(\mathbf{r})| / g)}{|\mathbf{k}_p(\mathbf{r})|} \right| \quad (21)$$

results in a bathymetry map.

As it was mentioned in the introduction, the wave-current interaction effect is commonly neglected in the nearshore area since the magnitude of the corresponding currents is assumed to be small. The long-shore component can be significant and normally does not affect the wavefield which is already refracted and is propagating almost shorewards. This is a common convention while talking in radar based bathymetry inversion. A more detailed discussion of this topic is summarized in Section 8.

It is important to notice that in the main features of the 2D RWBI is close to the previously developed FFT-based algorithms, which perform the one-pixel shift 3D FFT spectral analysis with an adaptive window size. The advantage of the new method is that it basically applies all this techniques automatically through the nature of the CWT analysis and the peak wavelength, which shortens as the depth reduces due to the shoaling process. The 2D RWBI method allows getting the results with the same pixel size as in the radar image. This happens because of the fact that the translation vector passes through the entire physical space domain with the pixel size-step. The new method also removes additional restrictions, such as e.g. assumption regarding the smallness of the wavevector's spatial gradient in (Hessner et al., 1999).

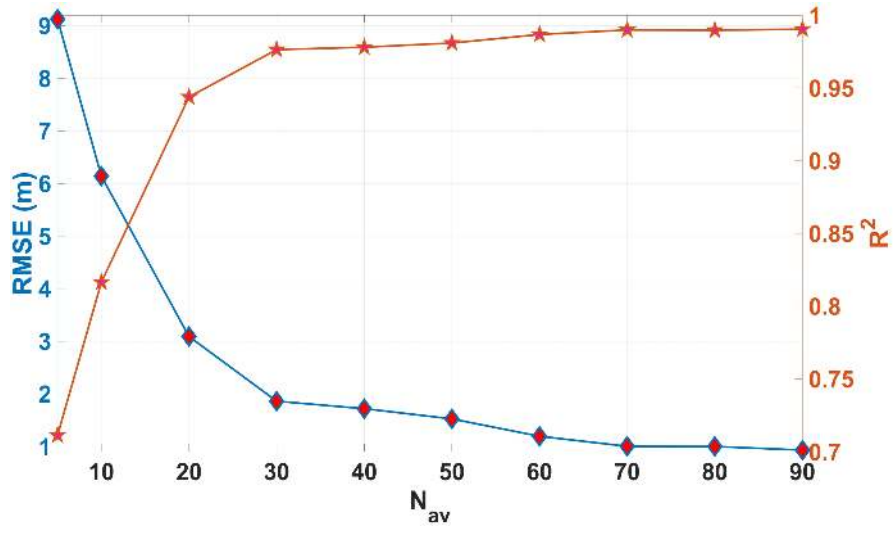


Figure 9: Dependence of the RMSE error in comparison to the linear regression model (see Figure 11 (c)) and the correlation coefficient on a number of averaged images (N_{av}). The dimensionless wavenumber $k_p h < 1$ was kept for all the calculations.

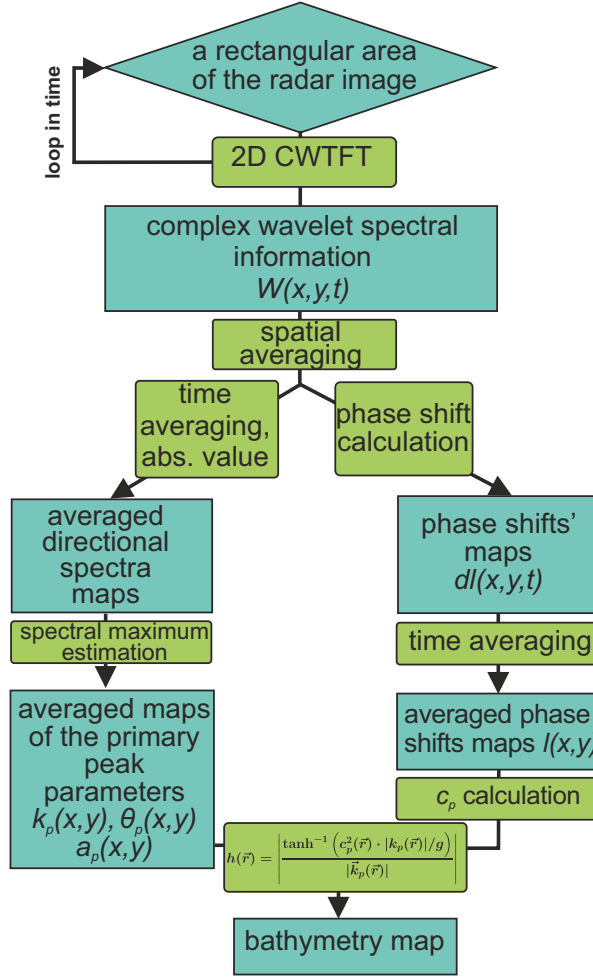


Figure 10: Block diagram of the bathymetry inversion process.

6. Analysis of the synthetic model results

In this section results obtained using the new method for the synthetic cases given above are presented and analyzed. Results of the reconstruction procedure, including the difference map, the scatter plot of the results and a comparison on a crosssection for $T_p = 10$ s are given in Figure 11. Obtained results demonstrate the ability of the proposed method to precisely retrieve bathymetry in the transition from intermediate to shallow water depths $k_p h < 1$. The corresponding bias on a lateral (y) coordinate slightly grows with depth as expected (see scatterplot in Figure 11 (c)). The deviation from the original at shallow depths might be addressed as an edge effect of the FFT used for calculations inside the 2D RCWBT. This kind of deviation appears at both edges, but the deeper edge was cut out due to the dimensionless wavenumber limit mentioned above.

The mean value and standard deviation of the difference array is defined as

$$M_{all}(\Delta) = \frac{1}{N_x N_y} \sum_{i=1}^{N_x} \sum_{j=1}^{N_y} \Delta(x_i, y_j), \quad (22)$$

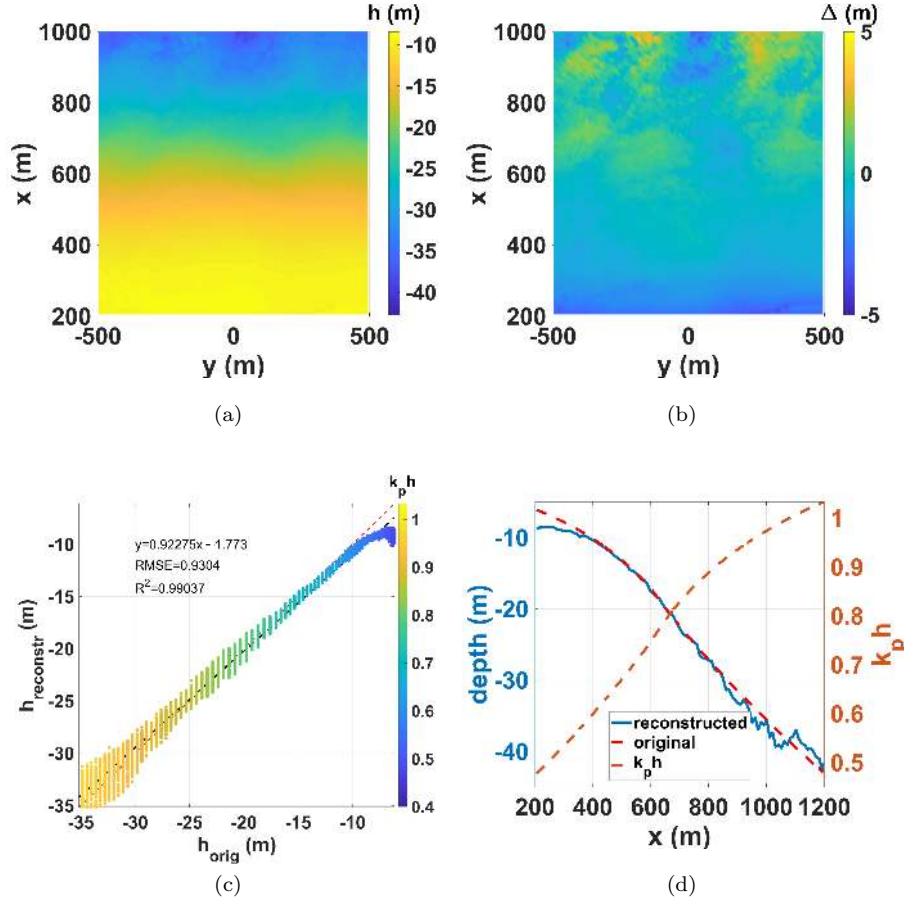


Figure 11: (a) Reconstructed water depth $h_{reconstr}(x, y)$; (b) difference map between original and reconstructed water depths; (c) scatterplot of the original and reconstructed bathymetries showing the lateral distribution of the retrieved results, as well as the growing error dispersion in deeper areas. The dashed red line is a bisecting line, the dashed black is the linear regression model. The well pronounced bias of the resulting bathymetry in shallow areas ($h < 10$ m) is generally due to the edge effect of the 2D CWTFT; (d) Comparison between original and reconstructed depths on the cross section $y = 0$

$$\sigma_{all}(\Delta) = \frac{1}{N_y} \sum_{i=1}^{N_y} \left(\frac{1}{N_x - 1} \sum_{j=1}^{N_x} \left| \Delta(x_j, y_i) - \frac{1}{N_x} \sum_{j=1}^{N_x} \Delta(x_j, y_i) \right|^2 \right)^{1/2}. \quad (23)$$

The corresponding statistical estimates of the comparison for this and other cases from the paper are summarized in Table 4.

255 7. Application to real data in Sylt island (Germany)

In order to evaluate results of the new method on real data, measurements from Sylt, a German barrier island in the North Sea, were analyzed. The typical coastline in the Western side of the island is a sandy, mixed energy coast (equally influenced by tidal currents and wave action). Both sub-tidal and inter-tidal sandbars are present along the islands West coast. They vary according to their cross-shore position and

260 extend depending on the particular alongshore location. Wind and waves are predominantly approaching from West. Tides in the area are semi-diurnal with a tidal range of about 2m.

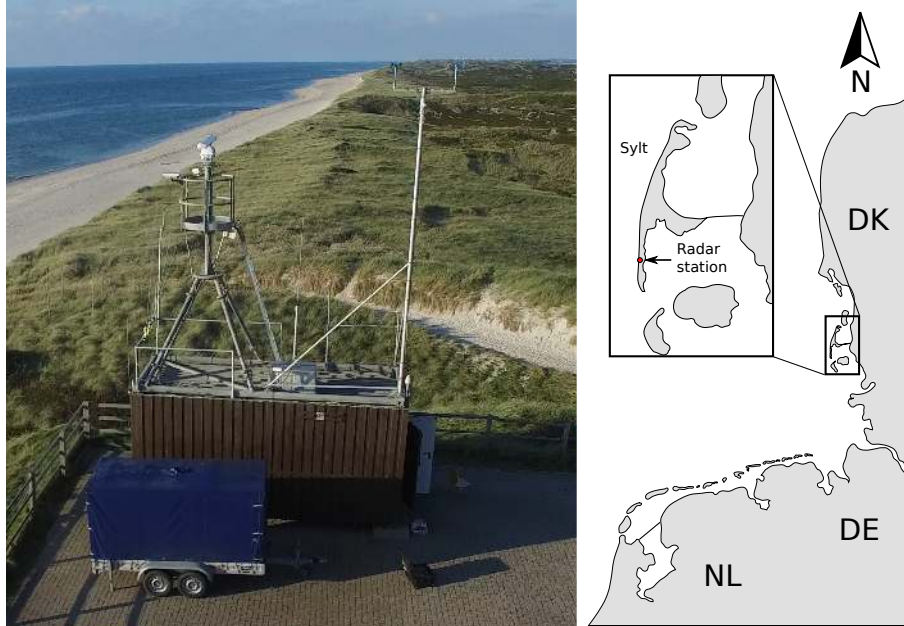


Figure 12: Illustration and location of the long-term radar and meteorology station. The station is located in the German Bight of the North Sea in the West coast of the German barrier island Sylt.

265 A long-term radar, sea state and meteorology station is operated by the Helmholtz-Zentrum Geesthacht (HZG) at the West coast of the island. Figure 12 illustrates the radar installation and the location of the study site within the German Bight. The station is part of the Coastal Observing System for Northern and Arctic Seas (COSYNA) (Baschek et al., 2017) and includes a weather station, a marine radar and a directional wave rider buoy. The buoy, a “Datawell Directional Wave Rider MkIII”, is moored 1.1 km away from the shoreline at a water depth of 10m. HZG’s coherent-on-receive marine radar (CMR) is operated at the land station. The height of the radar antenna for this installation is 28m above mean sea level. It is working at X-band (9.48 GHz) and consists of an off-the-shelf marine radar (GEM Leonardo series) equipped with a vertically polarized antenna in transmit and receive (VV). Technical details about the radar hardware and acquisition settings are listed in Table 2. A modification allows for a digitization and coherentization of the electromagnetic signal (see (Braun et al., 2008) (Seemann et al., 2017) for a description). However, for the present study, only incoherent radar data are analyzed.

270 The radar was set up to acquire 10 minutes of radar data with an antenna rotation frequency of ≈ 0.5 Hz at the beginning of each hour. For this study, one exemplary radar image sequence starting on September 29, 22:00 UTC was taken. The record represents the peak of a 4-days’ long storm event starting on September 27 and lasting until October 1, 2016. Water level and current information has been taken from the operational circulation model BSHmod operated by the German Federal Maritime and Hydrographic Agency (BSH). The water surface elevation at the time of the radar record was 1.6 m above mean sea level. A time close to slack tide was chosen to avoid current influences. A small onshore (eastward) directed current of 0.15 m/s was present, while alongshore currents were not present. The wave rider measured 2.98 m, 10 s and 282.7° for significant wave height, peak period and peak wave direction, respectively. The wind speed was measured to be 18 m/s from West at the time of the radar record. Figure 14 shows the wave spectrum recorded by the buoy, as well as a directional spectrum that was computed from the buoy motions using the WAFO toolbox (Brodtkorb et al., 2000) using 101 directional bins and a window length of 256 data points for the spectral analysis. The directional distribution of wave energy spreads from North West to South

West with the largest portion of energy coming from West. Reflection of wave energy is not apparent in the directional spectrum. This is expected for the dissipative, sandy beach at the study site. The tail of the wave spectrum indicates that the relatively shallow water depth of 10 to 12 m at the buoy location already influences the spectral shape (towards a TMA spectral shape). The information about the environmental conditions is also listed in Table 3.

The sea floor topography was mapped on September 22 - 26, 2016 from a small (7 m long) vessel equipped with a RTK-GPS system to track the ship motion and a 210 kHz single beam echo sounder. The dataset is available from the PANGEA data portal (Cysewski et al., 2019). The echo sounder transects were mapped to a 5 m by 5 m grid for a comparison with the radar derived bathymetry. Multiple pings within one grid cell were averaged first. Grid cells where no pings were available were filled by linear interpolation. Because the point density is much higher in the cross-shore direction, the linear interpolation was undertaken only in the alongshore direction. In the alongshore direction, the bathymetry dataset spans about 1.5 km to either side of the radar station and 3 km offshore. An alongshore subtidal sandbar with its bar crest at 4 m below Mean Sea Level (MSL) is present around 500 m away from the shore line. The trough between this sandbar and the intertidal zone lies around 6 m below MSL. From 1 km to further offshore the sea floor is quite constant at 10 to 12 m below MSL. There is evidence that tidally formed underwater sand dunes with amplitudes of ≈ 1 m are present in this area.

Table 2: Radar characteristics (signal, acquisition, probing geometry).

Parameter	Value
Frequency	9.48 (GHz)
Polarization	VV
Pulse Repetition Frequency (PRF)	2 (kHz)
Antenna rotation period	2 (s)
Antenna beam length	2.3 (m)
Azimuthal resolution	0.9°
Pulse length	50 - 70 (ns)
Sampling frequency / Range resolution	20 (MHz) / 7.5 (m)
Maximum range	3.262 (km)
Radar installation height	28 (m)

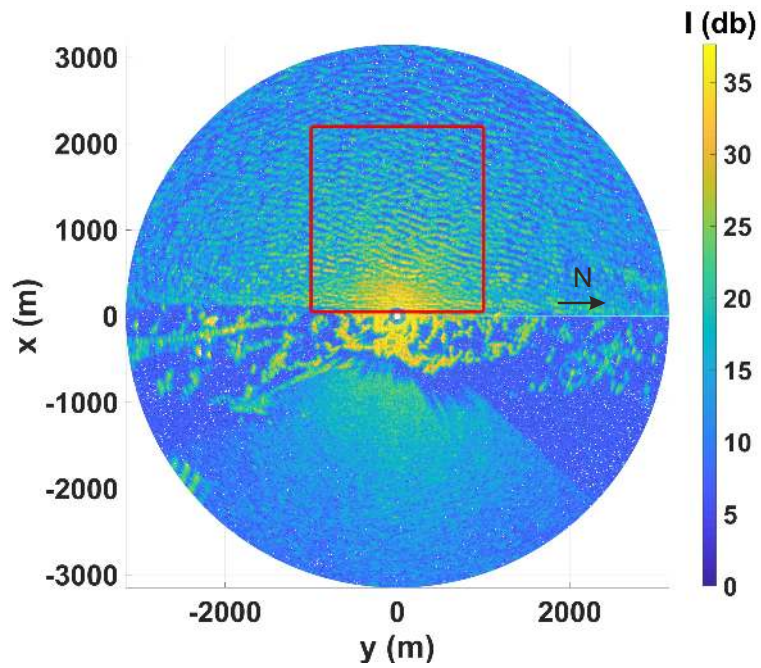


Figure 13: Example of real radar intensity image collected during the storm 29th of September 2016 Sylt island coast.

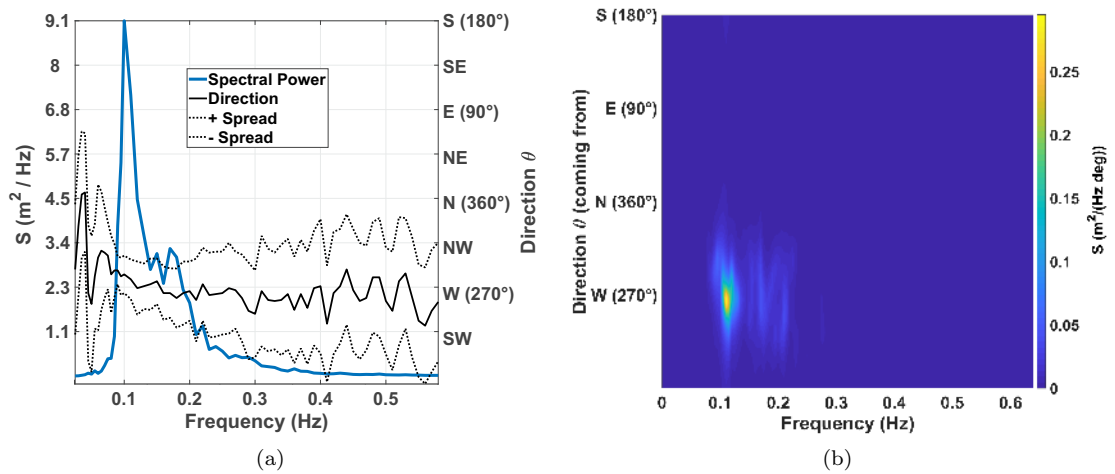


Figure 14: (a) Wave spectrum measured at 2016-09-29 22:12 (UTC) with frequency dependent wave direction (continuous black) and directional spread (dashed black) processed by the wave rider buoy; (b) directional spectrum estimated from the buoy motions using the WAFO toolbox (Brodtkorb et al., 2000).

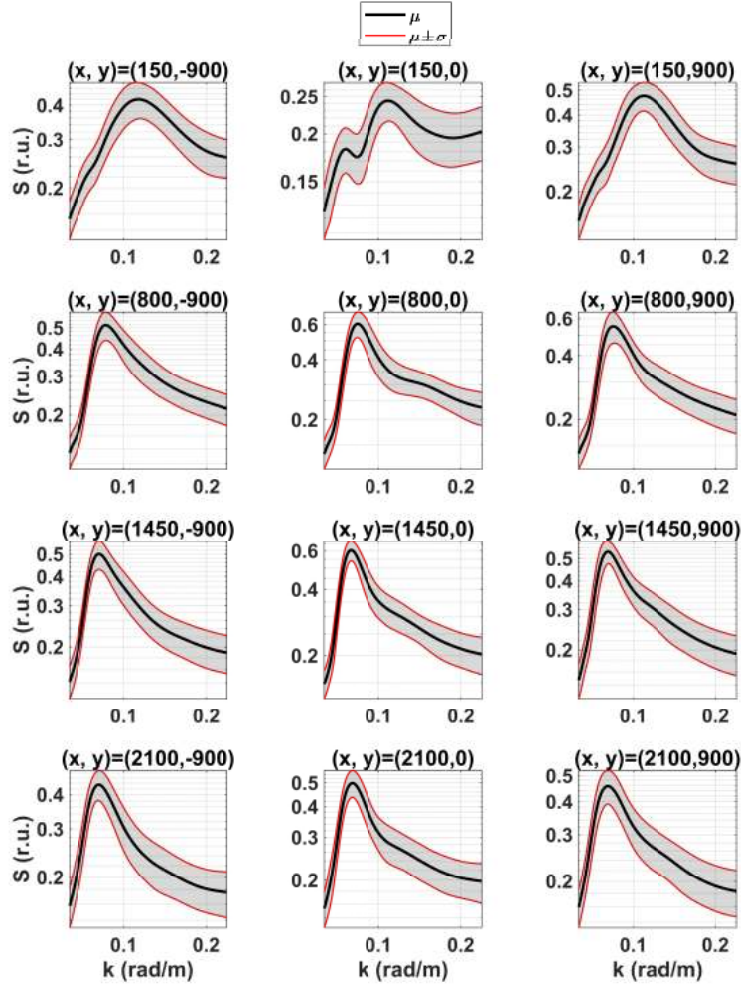


Figure 15: Wavelet analysis derived 1D omnidirectional spectra (Sylt island data) with the corresponding mean (black solid line μ) and standard deviation limits (gray zone with the red St.D. limits $\mu \pm \sigma$). Spectral values are given in a relative units (r.u.).

Table 3: Tide, sea state and wind at the time of the study.

ζ	u	v	H_s	T_p	θ_p	U_{10}
1.6 (m)	0.15 (m/s)	0.0 (m/s)	2.98 (m)	10 (s)	282.7°	18 (m/s)

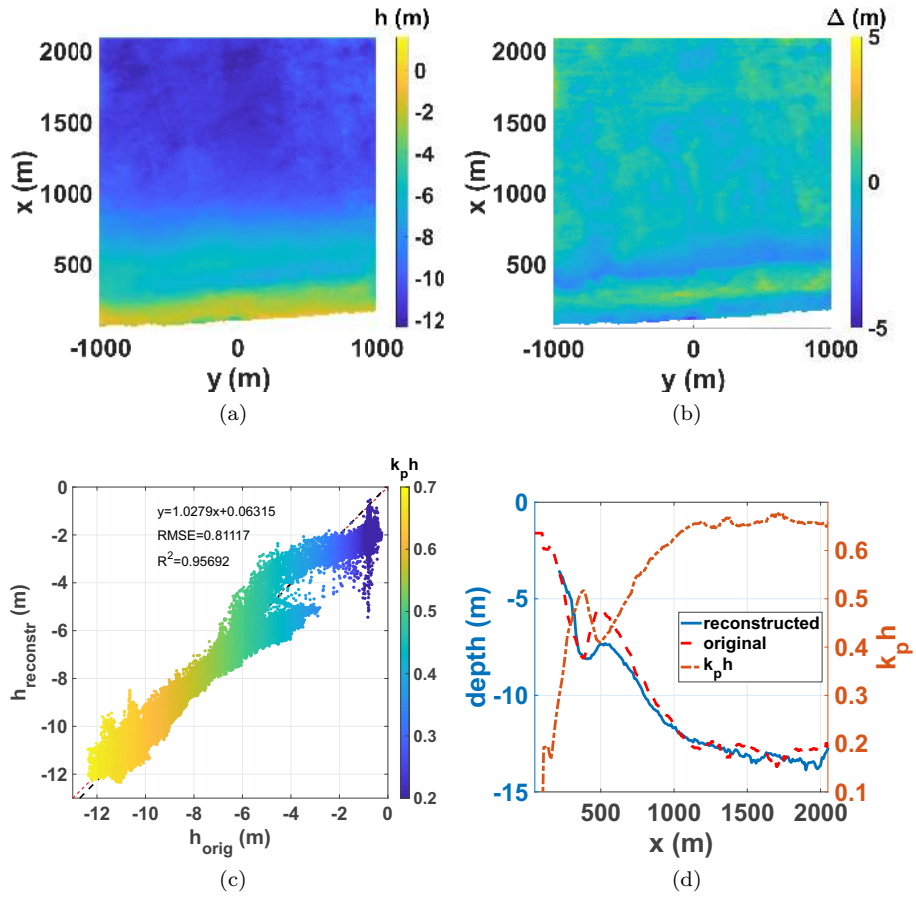


Figure 16: (a) Resulting map of the bathymetry reconstruction $h_{reconstr}(x, y)$; the whitened domain corresponds to the the area which is not covered by water, according to the prior calm conditions bathymetric survey (b) the resulting difference map while correcting the bathymetry survey only by computed tidal elevation differences and no other storm-related surges; (c) scatterplot of measured versus reconstructed bathymetry (d) comparison on a cross-section. Mean characteristics of the comparison are given in Table 4.

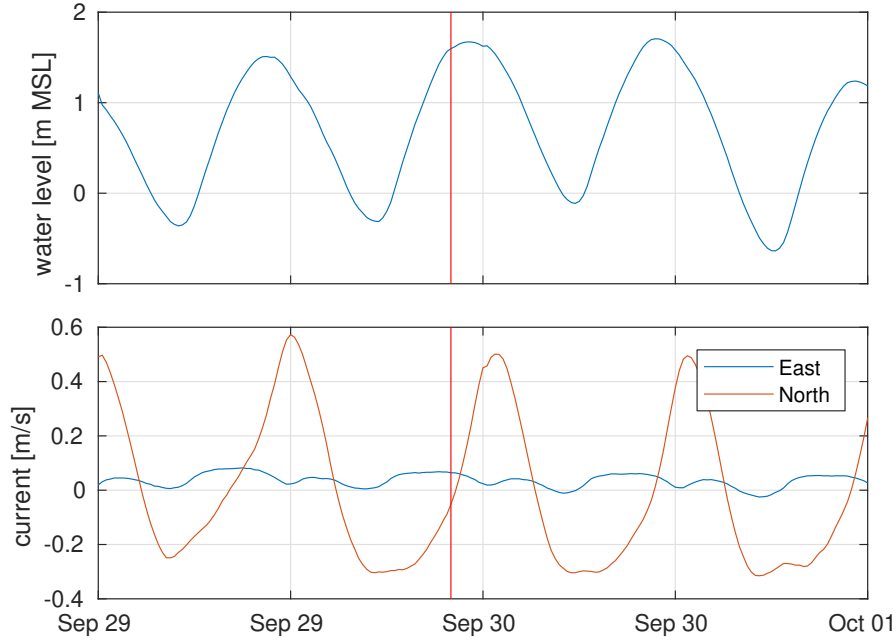


Figure 17: Water level tidal variation from the mean sea level (upper panel) and tidal current information (lower panel) in accordance with the operational circulation model BSHcmod operated by the German Federal Maritime and Hydrographic Agency. The data of the radar data acquisition is marked with a vertical red line.

Table 4: Mean characteristics of the result comparison

Case	$\sigma_{all}(\Delta)$ (m)	$M_{all}(\Delta)$ (m)	R^2
$T_p = 7$ s. (simul.)	1.16	1.28	0.8
$T_p = 10$ s. (simul.)	0.69	0.85	0.99
Sylt (real)	0.47	0.57	0.95
Sylt (simul.)	0.35	0.5	0.99
Steep bathymetry	1.53	2.07	0.99

8. Discussion and conclusions

305 A new 2D RWBI method was developed and verified both for synthetic and real X-band radar data. The method has shown to give robust results for inversion of the bathymetric maps in intermediate and shallow waters of $k_p h < 1$. The results show an improved or similar accuracy compared to previous measured and simulated findings of e.g. (Ludeno et al., 2018), where the RMSE was in the range 1.51 – 1.61 m with $R^2 \approx 0.94 - 0.96$.

310 The new 2D RWBI method has several advantages compared to dispersion relation cone fitting-based FFT methods. The 2D CWT approach is localized and hence naturally fits the inhomogeneous conditions found in the nearshore environment due to bathymetry changes and the wavefield’s evolution via shoaling. FFT-based methods assume homogeneity and periodicity in a rectangular area limiting their ability to account for rapid bathymetry changes.

315 The 2D CWT is continuous, i.e. the wavelet size is correlated with a peak wavelength and is smoothly changing due to the shoaling process and the translation vector passes over the entire physical space with the same pixel-size steps. It also uses additional wave phase information through the calculation of the corresponding lag in successive radar images allowing for an accurate estimation of the corresponding peak

component's celerity. This enables providing smooth bathymetry maps with relatively high depth accuracy. Furthermore, as it does not require the evaluation of frequency-wavenumber spectra, it does not need large integration times. This reduced integration time (few minutes) allows working in short time sequences with a potential to track the bathymetry evolution during storm events.

Another advantage of the 2D CWT method is that it is not limited to rectangular areas. It can process the entire radar panorama including arbitrary shapes defined by shorelines or structures without affecting the results. This means that one can take a rectangular crop of the radar image, which includes land and sea, process it, and apply the land/construction mask to the results *a-posteriori*.

The method allows to estimate the pair $(c_p(\mathbf{r}), \mathbf{k}_p(\mathbf{r}))$. Hence, in cases where external information about the current field $\mathbf{U}(\mathbf{r})$ in the area of processing (in-situ measurements, models, or independent radar-based estimation) is available, the corresponding Doppler shifts can be easily incorporated modifying the standard inversion Equation (21) in the following way

$$h(\mathbf{r}) = \left| \frac{\tanh^{-1} \left((c_p - \mathbf{k}_p \mathbf{U} / |\mathbf{k}_p|)^2(\mathbf{r}) |\mathbf{k}_p(\mathbf{r})| / g \right)}{|\mathbf{k}_p(\mathbf{r})|} \right|. \quad (24)$$

In addition, the inversion technique can be slightly modified in order to account for the mean current. For instance, several neighboring components - with the same wave number - on the spectral peak can be taken to estimate the corresponding celerities using steps 1-6 of the 2D RWBI algorithm and then fitting two components of currents assuming a weak change in the corresponding peak frequency $\omega(|\mathbf{k}_p|, \theta_p \pm \varepsilon) \approx \omega(|\mathbf{k}_p|, \theta_p)$. This approach can be implemented in future works for improving the method's performance and capability.

In order to apply the method in near-real time the relatively high computational resources needed in terms of RAM and HD volume should be addressed. In addition, despite the high resolution achieved by the method, further improvements are required to allow for a better detection of abrupt bottom changes such as nearshore sandbars, underwater rocks, etc. More precisely, small spatial bathymetry variations need to be tracked with the corresponding short wavelengths. This can be implemented in the proposed method either by using a data set with a higher primary peak or additional (secondary) peaks which coexist with the primary one, but are lower in amplitude and higher in wavenumber. If such features are located in deeper seas, it is important to ensure that both features and background are within the required dimensionless wavenumber limitation $kh < 1$ for any directional spectral component taken. In general, within single storm there is an evolution of peak frequency, which should enable extracting different regions within the radar footprint using the best available peak frequency and direction.

As in any new method, more work can be done in order to thoroughly investigate the bathymetry inversion of the nearshore sandbars. This area is challenging not only due to the reasons mentioned above, but also due to wave breaking, and to possible water column accelerations due to rapid depth changes. The present study excludes the surf zone from the analysis. Radar images solely are sufficient to provide the area of intensive breaking by analyzing the time-averaged intensity maps (Haller et al., 2013). As waves shoal and break on a beach, the momentum flux in the onshore direction is reduced resulting in compensating forces on the water column. The change of mean water level offshore the breaker line is described as a gradual reduction of the mean water level as the shoreline is approached. Inside the breaking zone, following the spilling breaking model, the wave field undergoes setup, which is linear with depth and approximately is on the level of 20 % of the breaking wave height (Dean and Dalrymple, 1991). For the conditions of the real data case described in Section 7 the corresponding correction is around 0.2-0.4 m. This might partially compensate the bias obtained in the real data case (see Figure 16) while comparing it to the calm conditions bathymetric survey. There also might be a storm surge which is typical of strong wind conditions, when the friction velocity u_* is close to 1.

Finally, it is important to point out that the high capabilities of the 2D RWBI method presented here are not limited to the use of X-band radar remote sensing. This method can fit for the analysis of other remote sensing equipment data such as other types of radars and optical cameras mounted on various platforms (Holman et al., 2017).

Appendix

365 An additional experiment was carried out to analyze more deeply the results of the real case presented in Section 7. A simulation case was built using the same method described in Section 2 with the following inputs. A JONSWAP spectrum ($T_p = 10$ s, $F = 500$ km, $U_{10} = 9.8$ m/s) was selected approximately fitting to the real conditions. The bathymetry was taken close to the original one but laterally uniform, and no currents were included. It can be seen from the simulation case results given in Figure 18 and Table 4 that the 2D RWBI method performs excellently up until the sandbar area.

370 It is worth noticing that the 2D RWBI method manages to locate the spectral peak and wave celerities providing good results in shallow waters. An exception is a limited area near the corners of the computation region, where it indicates its inability to provide the bottom depth estimation. Even in the synthetic reconstruction there is still under/overestimation of the rapidly changing features near the sandbar. It is lower than that found in the field which can be due to other mean water elevation changes such as storm surges and waves setup (see discussion in Section 8). The simulation case shows significantly smaller bias and RMSE in comparison to the real case both because a smaller area was taken and all the unwanted phenomena (radar equation, near zone of the radar, wave breaking, inhomogeneous current) were excluded from the analysis.

380 Another test was performed to estimate the ability of the method to deal with a steeper bathymetry. A JONSWAP spectrum was used ($T_p = 10$ s, $F = 300$ km, $U_{10} = 15$ m/s, $H_s(\mathbf{0}) = 5.32$ m, $\theta_p(\mathbf{0}) = -5^\circ$) and the following bottom profile

$$h(x, y) = \begin{cases} -3, & 400 \leq x \leq 500(\text{m}), \\ -0.1x + 50, & 550 \leq x \leq 700(\text{m}), \\ -25 & 750 \leq x \leq 1100(\text{m}) \end{cases} \quad (25)$$

with a spline-smoothed connections between the picewise-linear parts. This is an abruptly changing bathymetry with 10 % slope, which is less common for a typical sandy beaches. The method showed quite good depth estimation of the flat regions and the shallow slope within the limit of $k_p h < 1$. Nevertheless, some larger discrepancies are found near the connection of the slope to the deeper region (see Figure 19). Error statistics are summarized in Table 4.

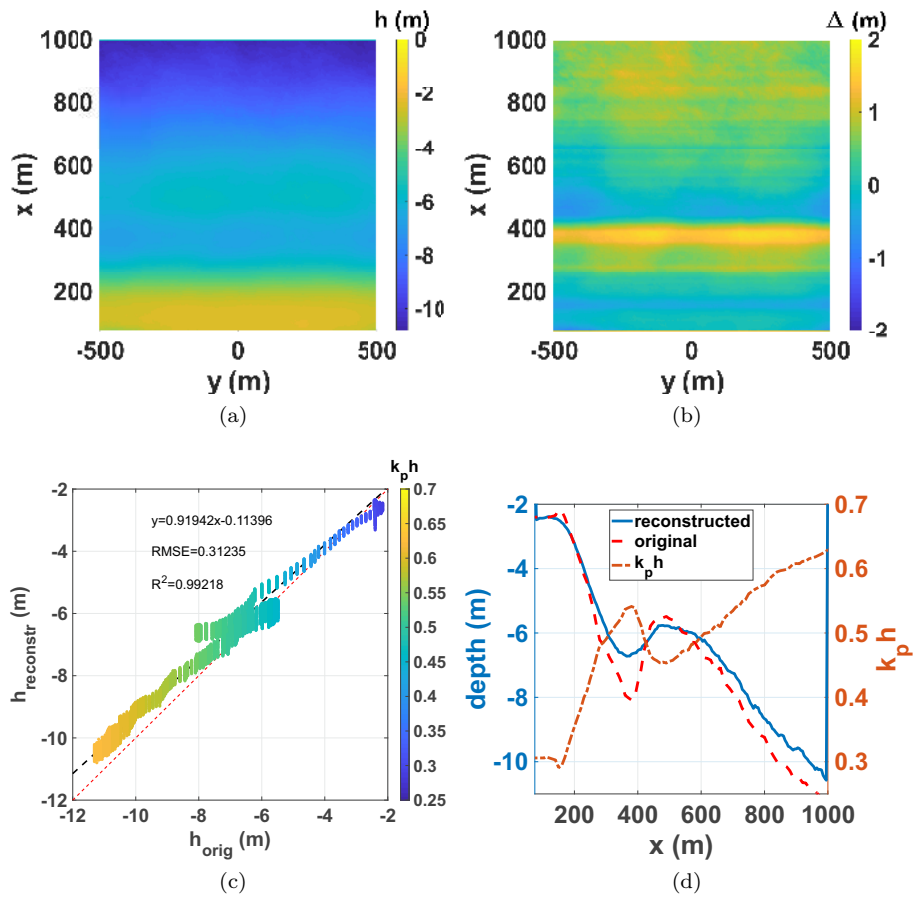


Figure 18: (a) Resulting map of the bathymetry reconstruction $h_{reconstr}(x, y)$ for the simulated Sylt bathymetry case; (b) resulting difference map: the systematic bias of the result is manifested on the outer sandbar area; (c) scatterplot of the reconstructed versus measured bathymetry (d) comparison on a cross-section. The mean characteristics of the comparison are given in Table 4.

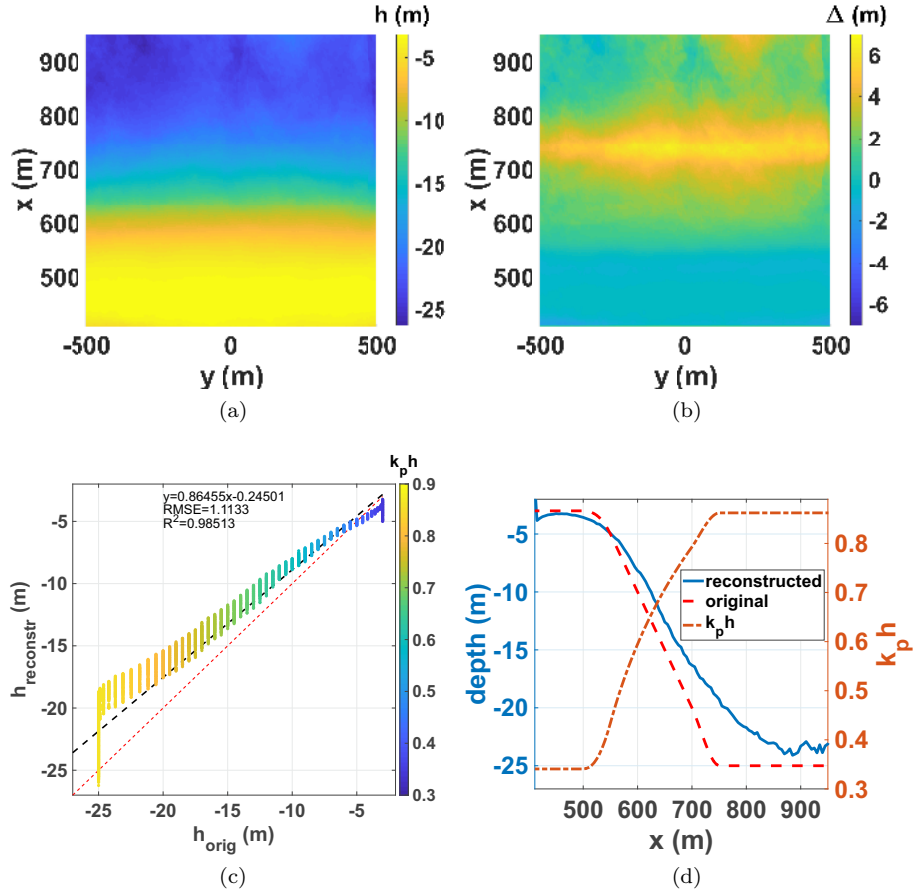


Figure 19: (a) Resulting map of the bathymetry reconstruction $h_{reconstr}(x, y)$ for the simulated steep bathymetry case (original bathymetry is given in Equation (25)); (b) difference map between the modelled and reconstructed bathymetry; (c) scatterplot of the comparison: systematic bias of the result is clearly visible and grows with depth maintaining maximum near transition from the flat deep area to the slope; (d) comparison on a cross-section. The mean characteristics of the comparison are summarized in Table 4.

Acknowledgment

The authors would like to thank Thorger Brüning from the German Federal Maritime and Hydrographic Agency (BSH) for extracting water levels and currents information from the operational circulation model BSHmod and Dr. Sara Nauri from School of Mechanical Engineering, Tel Aviv University for significant help in improving and editing the manuscript. The work was supported by the Israeli Ministry of Science and Technology and the German Federal Ministry of Education and Research (BMBF-MOST grant No. 3-15249) and Israeli Ministry of Science and Technology (grant No. 3-12473). P.C. would like to thank the Mediterranean Sea Research Center of Israel (MERCIS) for providing a travel grant to present the outcome of this research, Y.T. would like to thank the kind travel grant support of Alexander von Humboldt foundation.

395 **References**

- Abileah, R.. Mapping near shore bathymetry using wave kinematics in a time series of WorldView-2 satellite images. *International Geoscience and Remote Sensing Symposium (IGARSS) 2013*;2:2274–2277. doi:10.1109/IGARSS.2013.6723271.
- Abileah, R., Trizna, D.B.. Shallow water bathymetry with an incoherent X-band radar using small (smaller) space-time image cubes. *International Geoscience and Remote Sensing Symposium (IGARSS) 2010*;4330–4333doi:10.1109/IGARSS.2010.5654386.
- 400 Antoine, J.P., Murenzi, R.. Two-dimensional directional wavelets and the scale-angle representation. *Signal processing* 1996;52(3):259–281.
- Baschek, B., Schroeder, F., Brix, H., Riethmüller, R., Badewien, T.H., Breitbach, G., Brügge, B., Colijn, F., Doerffer, R., Eschenbach, C., et al. The coastal observing system for northern and arctic seas (cosyna). *Ocean Science* 2017;13(3):379–410.
- 405 Bell, P.S.. Bathymetry derived from an analysis of x-band marine radar images of waves. *Proc Oceanology '98* 1998;3:535–543.
- Bell, P.S.. Shallow water bathymetry derived from an analysis of X-band marine radar images of waves. *Coastal Engineering* 1999;37(3-4):513–527. doi:10.1016/S0378-3839(99)00041-1.
- Bell, P.S., Osler, J.C.. Mapping bathymetry using X-band marine radar data recorded from a moving vessel. *Ocean Dynamics* 2011;61(12):2141–2156. doi:10.1007/s10236-011-0478-4.
- 410 Birkemeier, W.A., Mason, C.. The crab: A unique nearshore surveying vehicle. *Journal of Surveying Engineering* 1984;110(1):1–7.
- Borge, J.C.N., Rodríguez, G.R., Hessner, K., González, P.I.. Inversion of marine radar images for surface wave analysis. *Journal of Atmospheric and Oceanic Technology* 2004;21(8):1291–1300.
- Braun, N., Ziemer, F., Bezuglov, A., Cysewski, M., Schymura, G.. Sea-surface current features observed by doppler radar. *IEEE Transactions on Geoscience and Remote Sensing* 2008;46(4):1125–1133.
- 415 Bredmose, H., Agnon, Y., Madsen, P., Schäffer, H.. Wave transformation models with exact second-order transfer. *European Journal of Mechanics - B/Fluids* 2005;24(6):659–682. URL: <https://www.sciencedirect.com/science/article/pii/S0997754605000609>. doi:10.1016/J.EUROMECHFLU.2005.05.001.
- Brodtkorb, P., Johannesson, P., Lindgren, G., Rychlik, I., Rydén, J., Sjö, E.. WAFO - a Matlab toolbox for the analysis of random waves and loads. In: *Proc. 10th Int. Offshore and Polar Eng. Conf., ISOPE, Seattle, USA. volume 3; 2000. p. 343–350.*
- 420 Bruun, P.. Coast erosion and the development of beach profiles. volume 44. US Beach Erosion Board, 1954.
- Chernyshov, P., Vrecica, T., Toledo, Y.. Inversion of nearshore x-band radar images to sea surface elevation maps. *Remote Sensing* 2018;10(12). URL: <http://www.mdpi.com/2072-4292/10/12/1919>. doi:10.3390/rs10121919.
- 425 Chuang, L.Z.H., Wu, L.C., Doong, D.J., Kao, C.C.. Two-dimensional continuous wavelet transform of simulated spatial images of waves on a slowly varying topography. *Ocean Engineering* 2008;35(10):1039–1051. doi:10.1016/j.oceaneng.2008.02.008.
- Cysewski, M., Streßer, M., Bödewadt, J., Perthun, P., Carrasco, R., Horstmann, J.. Single beam bathymetry transects at the West coast of Sylt from Sep 22-26 2016. 2019. URL: <https://doi.pangaea.de/10.1594/PANGAEA.898407>.
- 430 Daubechies, I.. Ten lectures on wavelets. SIAM, 1992.
- Dean, R.G., Dalrymple, R.A.. *Water wave mechanics for engineers and scientists. volume 2.* world scientific publishing Co Inc, 1991.
- Haller, M.C., Honegger, D., Catalan, P.A.. Rip current observations via marine radar. *Journal of waterway, port, coastal, and ocean engineering* 2013;140(2):115–124.
- 435 Hart, C., Miskin, E.. Developments in the method of determination of beach gradients by wave velocities. Air survey research paper no 15, Directorate of Military Survey, UK War Office 1945;.
- Hasselmann, K., Barnett, T., Bouws, E., Carlson, H., Cartwright, D., Enke, K., Ewing, J., Gienapp, H., Hasselmann, D., Kruseman, P., Meerburg, A., Müller, P., Olbers, D., Richter, K., Sell, W., Walden, H.. Measurements of wind-wave growth and swell decay during the Joint North Sea Wave Project (JONSWAP). *Ergänzungsheft 8-12* 1973;URL: <https://repository.tudelft.nl/islandora/object/uuid:f204e188-13b9-49d8-a6dc-4fb7c20562fc/>.
- 440 Hessner, K., Reichert, K., Rosenthal, W.. Mapping of sea bottom topography in shallow seas by using a nautical radar. In: *2nd Symposium on Operationalization of Remote Sensing. 1999. .*
- Holman, R., Plant, N., Holland, T.. CBathy: A robust algorithm for estimating nearshore bathymetry. *Journal of Geophysical Research: Oceans* 2013;118(5):2595–2609. doi:10.1002/jgrc.20199.
- 445 Holman, R.A., Brodie, K.L., Spore, N.J.. Surf zone characterization using a small quadcopter: technical issues and procedures. *IEEE Transactions on Geoscience and Remote Sensing* 2017;55(4).
- Honegger, D.A.. *Depth estimation and frontal imaging via X-band marine radar. Ph.D. thesis; Civil and Construction Engineering; 2015.*
- Hoogeboom, F., Kleijweg, J., Halsema, D.v.. *Seawave measurements using a ships radar. ESA; 1986. .*
- 450 Huang, W., Carrasco, R., Shen, C., Gill, E.W., Horstmann, J.. Surface current measurements using X-band marine radar with vertical polarization. *IEEE Transactions on Geoscience and Remote Sensing* 2016;54(5):2988–2997. doi:10.1109/TGRS.2015.2509781.
- Kanevsky, M.B.. *Radar imaging of the ocean waves. Elsevier, 2008.*
- Kennedy, A., Dalrymple, R., Kirby, J., Chen, Q.. Determination of inverse depths using direct boussinesq modeling. *Journal of Waterway, Port, Coastal, and Ocean Engineering* 2000;126(4):206–214.
- 455 Litvenko, K.V., Prigarin, S.M.. The error analysis for spectral models of the sea surface undulation. *Russian Journal of Numerical Analysis and Mathematical Modelling* 2014;29(4):239–250.
- Ludeno, G., Postacchini, M., Natale, A., Brocchini, M., Lugni, C., Soldovieri, F., Serafino, F.. *Normalized Scalar*

- Product Approach for Nearshore Bathymetric Estimation from X-Band Radar Images: An Assessment Based on Simulated and Measured Data. *IEEE Journal of Oceanic Engineering* 2018;43(1):221–237. doi:10.1109/JOE.2017.2758118.
- 460 Ludeno, G., Reale, F., Dentale, F., Carratelli, E.P., Natale, A., Soldovieri, F., Serafino, F.. An X-band radar system for bathymetry and wave field analysis in a harbour area. *Sensors (Switzerland)* 2015;15(1):1691–1707. doi:10.3390/s150101691.
- Mitsuyasu, H., Tasai, F., Suhara, T., Mizuno, S., Ohkusu, M., Honda, T., Rikiishi, K.. Observations of the directional spectrum of ocean Waves Using a cloverleaf buoy. *Journal of Physical Oceanography* 1975;5:750–760.
- 465 Piotrowski, C.C., Dugan, J.P.. Accuracy of bathymetry and current retrievals from airborne optical time-series imaging of shoaling waves. *IEEE Transactions on Geoscience and Remote Sensing* 2002;40(12):2606–2618.
- Poupardin, A., Idier, D., De Michele, M., Raucoules, D.. Water depth inversion from a single spot-5 dataset. *IEEE Transactions on Geoscience and Remote Sensing* 2016;54(4):2329–2342.
- Rutten, J., De Jong, S.M., Ruessink, G.. Accuracy of nearshore bathymetry inverted from X-band radar and optical video data. *IEEE Transactions on Geoscience and Remote Sensing* 2017;55(2):1106–1116.
- 470 Salcedo-Sanz, S., Borge, J.N., Carro-Calvo, L., Cuadra, L., Hessner, K., Alexandre, E.. Significant wave height estimation using svr algorithms and shadowing information from simulated and real measured x-band radar images of the sea surface. *Ocean Engineering* 2015;101:244–253.
- Seemann, J., Carrasco, R., Stresser, M., Horstmann, J., St, S., Trulsen, K., Borge, J.N., et al. An operational wave monitoring system based on a dopplerized marine radar. In: *OCEANS 2017-Aberdeen*. IEEE; 2017. p. 1–4.
- 475 Senet, C.M., Seemann, J., Flampouris, S., Ziemer, F.. Determination of bathymetric and current maps by the method DiSC based on the analysis of nautical X-band radar image sequences of the sea surface (November 2007). *IEEE Transactions on Geoscience and Remote Sensing* 2008;46(8):2267–2279. doi:10.1109/TGRS.2008.916474.
- Serafino, F., Lugni, C., Nieto Borge, J.C., Zamparelli, V., Soldovieri, F.. Bathymetry determination via X-band radar data: A new strategy and numerical results. *Sensors* 2010;10(7):6522–6534.
- 480 Skolnik, M.I.. *Radar handbook*, 1970.
- Wang, L., Wu, X., Pi, X., Ma, K., Liu, J., Tian, Y.. Numerical simulation and inversion of offshore area depth based on X-band microwave radar. *Acta Oceanologica Sinica* 2015;34(3):108–114. URL: <http://link.springer.com/10.1007/s13131-015-0626-7>. doi:10.1007/s13131-015-0626-7.
- 485 Wang, N., Lu, C.. Two-dimensional continuous wavelet analysis and its application to meteorological data. *Journal of atmospheric and oceanic technology* 2010;27(4):652–666.
- Wu, L.C., Chuang, L.Z.H., Doong, D.J., Kao, C.C.. Quantification of non-homogeneity from ocean remote-sensing images using two-dimensional continuous wavelet transforms. *International journal of remote sensing* 2011;32(5):1303–1318.

List of Figure Captions

- 490 1. Flowchart of the peak elimination method for **(a)** frequency definition and for **(b)** direction definition.
2. Point plot of the discretized wave spectra. The spectra is discretized in four thousand frequency directional bins, as outlined in Section 3. The color indicates the energy density at each point.
3. Bathymetry profile according to Equation (5) as a function of the simulation (x_{simul}) coordinate and the corresponding x coordinate for radar image construction stage (x_{radar}). The green extension of the original equilibrium profile shows how it evolves to the zero depth. Red vertical lines denote the change of the profile type and the offset R_0 used in the radar image simulation.
- 495 4. **(a)** An example of JONSWAP spectrum-based 2D shoaling wavefield (bottom view); **(b)** The bathymetry profile defined in equation (5) (dash-dotted blue line), the relative water depth ($k_p h$) (dashed orange line), and 1D sea surface elevation (solid blue line). The coordinate system is already changed to radar one as described in Figure 3. The shortening of the wavelength together with a mild amplitude modulation is clearly visible while entering shallower waters.
- 500 5. **(a)** Probing geometry scheme including the illustration of shadowing and tilt modulation as a scalar product of the unitary external normal vector \mathbf{n} and the unitary vector pointing to the radar antenna \mathbf{u} ; **(b)** An example of radar image with $H_r = 20$ m, noise level 5 % (intensity is given in relative units). Stars and numbers correspond to the numbering of probing locations for 2D CWTFIT, given in Figure (7).
- 505 6. **(a)** Original Morlet wavelet in the physical (x, y) space (see Equation 14); **(b)** The same Morlet wavelet rotated ($\alpha = \pi/7$) and translated $\mathbf{b} = (2, 2)$.
7. The wavelet spectra of the radar image, averaged over one hundred time samples (200 s). The numbering corresponds to the probing locations given in Figure 5 (b). All the phenomena taken into account in the simulations are obviously visible: refraction (the incidence angle tends to decrease), shoaling (wave shortening - wavenumber growth), the second harmonic due to the presence of shadowing is also clearly seen.
8. The 1D omnidirectional (spectral angle-integrated) wavelet spectra with the corresponding mean (black solid line μ) and standard deviation limits (gray zone with the red St.D. limits $\mu \pm \sigma$). The order of spectra corresponds to that in Figure 7. Spectral values are given in relative units (r.u.).
- 515 9. Dependence of the RMSE error in comparison to the linear regression model (see Figure 11 (c)) and the correlation coefficient on a number of averaged images (N_{av}). The dimensionless wavenumber $k_p h < 1$ was kept for all the calculations.
- 520 10. Block diagram of the bathymetry inversion process.
11. **(a)** Reconstructed water depth $h_{reconstr}(x, y)$; **(b)** difference map between original and reconstructed water depths; **(c)** scatterplot of the original and reconstructed bathymetries showing the lateral distribution of the retrieved results, as well as the growing error dispersion in deeper areas. The dashed red line is a bisecting line, the dashed black is the linear regression model. The well pronounced bias of the resulting bathymetry in shallow areas ($h < 10$ m) is generally due to the edge effect of the 2D CWTFIT; **(d)** Comparison between original and reconstructed depths on the cross section $y = 0$
- 525 12. Illustration and location of the long-term radar and meteorology station. The station is located in the German Bight of the North Sea in the West coast of the German barrier island Sylt.
13. Example of real radar intensity image collected during the storm 29th of September 2016 Sylt island coast.
- 530 14. **(a)** Wave spectrum measured at 2016-09-29 22:12 (UTC) with frequency dependent wave direction (continuous black) and directional spread (dashed black) processed by the wave rider buoy; **(b)** directional spectrum estimated from the buoy motions using the WAFO toolbox (Brodtkorb et al., 2000).
15. Wavelet analysis derived 1D omnidirectional spectra (Sylt island data) with the corresponding mean (black solid line μ) and standard deviation limits (gray zone with the red St.D. limits $\mu \pm \sigma$). Spectral values are given in a relative units (r.u.).
- 535 16. **(a)** Resulting map of the bathymetry reconstruction $h_{reconstr}(x, y)$; the whitened domain corresponds to the the area which is not covered by water, according to the prior calm conditions bathymetric

- 540 survey(**b**) the resulting difference map while correcting the bathymetry survey only by computed tidal elevation differences and no other storm-related surges; (**c**) scatterplot of measured versus reconstructed bathymetry (**d**) comparison on a cross-section. Mean characteristics of the comparison are given in Table 4.
- 545 17. Water level tidal variation from the mean sea level (upper panel) and tidal current information (lower panel) in accordance with the operational circulation model BSHcmod operated by the German Federal Maritime and Hydrographic Agency. The data of the radar data acquisition is marked with a vertical red line.
- 550 18. (**a**) Resulting map of the bathymetry reconstruction $h_{reconstr}(x, y)$; the whitened domain corresponds to the the area which is not covered by water, according to the prior calm conditions bathymetric survey(**b**) the resulting difference map while correcting the bathymetry survey only by computed tidal elevation differences and no other storm-related surges; (**c**) scatterplot of measured versus reconstructed bathymetry (**d**) comparison on a cross-section. Mean characteristics of the comparison are given in Table 4.
- 555 19. (**a**) Resulting map of the bathymetry reconstruction $h_{reconstr}(x, y)$ for the simulated steep bathymetry case (original bathymetry is given in Equation (25)); (**b**) difference map between the modelled and reconstructed bathymetry; (**c**) scatterplot of the comparison: systematic bias of the result is clearly visible and grows with depth maintaining maximum near transition from the flat deep area to the slope; (**d**) comparison on a cross-section. The mean characteristics of the comparison are summarized in Table 4.